ACS APPLIED MATERIALS & INTERFACES

Research Article

Cite This: ACS Appl. Mater. Interfaces 2019, 11, 21454−21464

www.acsami.org

$La_{1.5}Sr_{0.5}NiMn_{0.5}Ru_{0.5}O_6$ Double Perovskite with Enhanced ORR/OER Bifunctional Catalytic Activity

Maria Retuerto,*[,†] Federico Calle-Vallejo,[‡] Laura Pascual,[§] Gunnar Lumbeeck,[∥] María Teresa Fernandez-Diaz,[⊥] Mark Croft,[#] Jagannatha Gopalakrishnan,[¶] Miguel A. Peña,[†] Joke Hadermann,[∥] Martha Greenblatt,[▽] and Sergio Rojas*[,†]

[†]Grupo de Energía y Química Sostenibles, Instituto de Catálisis y Petroleoquímica, and [§]Instituto de Catálisis y Petroleoquímica, CSIC, C/Marie Curie 2, L10, 28049 Madrid, Spain

[‡]Departament de Ciència de Materials i Química Fisica & Institut de Química Teòrica i Computacional (IQTCUB), Universitat de Barcelona, Martí i Franqués 1, 08028 Barcelona, Spain

[∥]EMAT, University of Antwerp, Groenenborgerlaan 171, 2020 Antwerp, Belgium

[⊥]Institut Laue-Langevin, BP156X, F-38042 Grenoble, France

[#]Department of Physics, Rutgers, The State University of New Jersey, 610 Taylor Road, Piscataway, New Jersey 08854, United States

[¶]Solid State and Structural Chemistry Unit, Indian Institute of Science, 560 012 Bangalore, India

[▽]Department of Chemistry and Chemical Biology, Rutgers, The State University of New Jersey, 610 Taylor Road, Piscataway, New Jersey 08854, United States

Supporting Information

ABSTRACT: Perovskites (ABO_3) with transition metals in active B sites are considered alternative catalysts for the water oxidation to oxygen through the oxygen evolution reaction (OER) and for the oxygen reduction through the oxygen reduction reaction (ORR) back to water. We have synthesized a double perovskite ($A_2BB'O_6$) with different cations in A, B, and B′ sites, namely, $(La_{1.5}Sr_{0.5})_A(Ni_{0.5}Mn_{0.5})_B(Ni_{0.5}Ru_{0.5})_{B'}O_6$ (LSNMR), which displays an outstanding OER/ORR bifunctional performance. The composition and structure of the oxide has been determined by powder X-ray diffraction, powder neutron diffraction, and transmission electron microscopy to be monoclinic with the space group $P2_1/n$ and with cationic ordering between the ions in the B and B′ sites. X-ray absorption near-edge spectroscopy suggests that LSNMR presents a configuration of ~Ni^{2+}, ~Mn^{4+}, and ~Ru^{5+}. This bifunctional catalyst is endowed with high ORR and OER activities in alkaline media, with a remarkable bifunctional index value of ~0.83 V (the difference between the potentials measured at −1 mA cm^{-2} for the ORR and +10 mA cm^{-2} for the OER). The ORR onset potential (E_{onset}) of 0.94 V is among the best reported to date in alkaline media for ORR-active perovskites. The ORR mass activity of LSNMR is 1.1 A g^{-1} at 0.9 V and 7.3 A g^{-1} at 0.8 V. Furthermore, LSNMR is stable in a wide potential window down to 0.05 V. The OER potential to achieve a current density of 10 mA cm^{-2} is 1.66 V. Density functional theory calculations demonstrate that the high ORR/OER activity of LSNMR is related to the presence of active Mn sites for the ORR- and Ru-active sites for the OER by virtue of the high symmetry of the respective reaction steps on those sites. In addition, the material is stable to ORR cycling and also considerably stable to OER cycling.

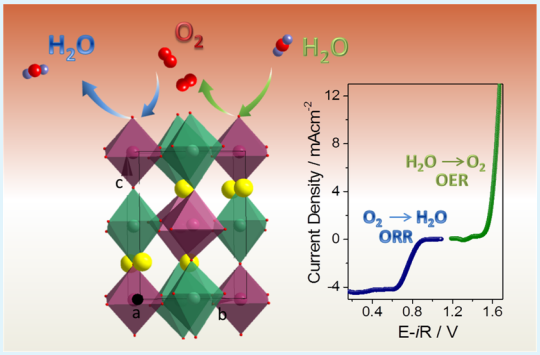

KEYWORDS: *regenerative fuel cells, metal−air batteries, bifunctional catalyst, OER, ORR, double perovskite*

INTRODUCTION

The term bifunctional catalyst applies to catalysts with measurable activity for the forward and reverse reactions. More than a mere curiosity, bifunctional catalysts are the holy grail for certain technological applications. For instance, they are essential for regenerative fuel cells and metal−air batteries. A regenerative fuel cell is an electrochemical device that combines O_2 and H_2 to produce H_2O ($O_2 + 2H_2 \rightarrow 2H_2O$) and generates electricity in the forward operation mode. In the reverse mode, the regenerative cell works as an electrolyzer, wherein electricity is used to split H_2O into O_2 and H_2 ($2H_2O \rightarrow O_2 + 2H_2$). The more demanding reactions in regenerative fuel cells are the ones involving oxygen, that is, oxygen reduction [$O_2 + 2H_2O + 4e^- \rightarrow 4OH^-$, denoted as oxygen

Received: February 4, 2019
Accepted: May 20, 2019
Published: May 22, 2019

DOI: 10.1021/acsami.9b02077
ACS Appl. Mater. Interfaces 2019, 11, 21454−21464

reduction reaction (ORR)] and oxygen evolution [$4OH^- \rightarrow O_2 + 2H_2O + 4e^-$, denoted as oxygen evolution reaction (OER)], in alkaline media. Therefore, regenerative fuel cells require bifunctional catalysts with low overpotentials and high catalytic activity and stability for the ORR and OER.[1−4]

In the case of metal−air batteries, a bifunctional catalyst for air cathodes would carry out the OER during the battery charge and the ORR during discharge, avoiding the development of cathodes based on two different catalysts, which is a complex task.[5−7] Thus, bifunctional catalysts could reduce costs and enhance the stability of batteries.[8]

Although the ORR and OER involve the same reactants and products, namely, H_2O, H_2, and O_2, the design of active and effective bifunctional catalysts is not trivial. Catalysts usually display considerably large overpotentials for both reactions and often a given material catalyzes one reaction more efficiently than the other. It is common that active catalysts for the ORR are not active for the OER and vice versa. For example, IrO_x-based compounds are the state-of-the-art OER catalysts in acid media, but they are not active for the ORR.[9,10] Conversely, Pt-based materials or Fe/N/C are the state-of-the-art materials for the ORR, but their activity for the OER is low or null.[11−14]

Therefore, it is highly desirable yet remarkably challenging to develop bifunctional catalysts with high activity and stability for the ORR and OER. A metric for bifunctionality was proposed by Schuhmann and co-workers,[15,16] which we will refer to here as the bifunctionality index (BI). This index is defined as the difference between the potentials required to reach an OER current density of 10 mA cm^{-2} and an ORR current density of −1 mA cm^{-2}. Although an ideal ORR−OER bifunctional catalyst would have a BI of ∼0 V, most catalysts display BIs larger than 1.0 V, and state-of-the-art bifunctional catalysts have values circa 0.9 V. Binary oxides, except for MnO_x,[17] display high BIs. Thus, mixed oxides have been reported as possible bifunctional candidates, especially in alkaline media, because their cost is substantially lower than noble metals and fairly high activities for both reactions have been measured.[18−20] Another definition for BI is the potential gap between 10 mA cm^{-2} for OER and −3 mA cm^{-2} for ORR (which should be a current density close to $E_{1/2}$ in perovskites).[21]

The bifunctional character of mixed oxides is owed to the versatile adjustment of the oxidation state of the metal cations depending on the adsorbed intermediate species. The most active mixed oxides display perovskite, spinel, or pyrochlore structures, with the transition metals in the structure considered to be the active sites. Perovskites including $LaNiO_3$, $La_{0.6}Ca_{0.4}CoO_3$, $La_{0.6}Ca_{0.4}MnO_3$, and $Ba_{0.5}Sr_{0.5}Co_{0.8}Fe_{0.2}O_3$ have been reported as active ORR−OER bifunctional catalysts.[22−25] Generally, the active cations are Ni, Co, Mn, or Ru, at the B sites of ABO_3 perovskites. In addition, Co-based spinel oxides are active for both reactions[26] and so are Ru- and Ir-based pyrochlores.[27]

In this work, we have synthesized and tested an ORR−OER bifunctional electrocatalyst with a remarkable BI value of ∼0.83. Our approach takes advantage of the flexibility of the perovskite structure to host cations with different oxidation states and catalytic characteristics. Following a strategy previously reported, based on doping ABO_3 with several cations in the A and B sublattices,[16] our bifunctional catalyst is based on the double perovskite $La_{1.5}Sr_{0.5}NiMn_{0.5}Ru_{0.5}O_6$ (denoted as LSNMR) in which Ni, Mn, and Ru cations occupy the B positions and La and Sr occupy the A positions. This bifunctional catalyst presents high ORR and OER activities in alkaline media. Furthermore, LSNMR is stable at potentials as low as 0.05 V versus reversible hydrogen electrode (RHE), at which the stability of most oxides is usually compromised. Density functional theory (DFT) calculations show that Mn sites are active for the ORR while Ru sites are active for the OER.

EXPERIMENTAL SECTION

Material Synthesis. LSNMR has been prepared by a solid-state reaction. The starting materials, namely, La_2O_3 (previously heated at 1000 °C), $SrCO_3$, NiO, MnO, and RuO_2, are mixed in stoichiometric proportions, ground, and thermally treated at 900 °C for 12 h in air. Subsequently, the powders are ground again and heated at 1200 °C in air for 12 h to obtain the pure double perovskite.

Material Characterization. The phase identification and purity was determined by powder X-ray diffraction (XRD) in Bragg−Brentano reflection geometry with Cu Kα radiation (λ = 1.5418 Å). A detailed crystallographic study was performed by powder neutron diffraction (PND). PND patterns were collected at room temperature on a D2B diffractometer with λ = 1.594 Å at the Institut Laue−Langevin (ILL) in Grenoble, France. The PND patterns were analyzed with the Rietveld method[28] using the Fullprof program.[29] In the refinements, the shape of the peaks was simulated by a pseudo-Voigt function. In the final run, the following parameters were refined: scale factor, background coefficients, zero-point error, unit cell parameters, pseudo-Voigt corrected for asymmetry parameters, positional coordinates, isotropic thermal factors, and relative cationic occupancy factor.

The specific surface area was determined from N_2 adsorption−desorption isotherms recorded at liquid N_2 temperature with a Micromeritics ASAP 2000 apparatus. The sample was degassed at 140 °C for 24 h under vacuum. The specific area was calculated by applying the Brunauer−Emmett−Teller (BET) method within the relative pressure range P/P_0 = 0.05−0.30.

The samples for transmission electron microscopy (TEM) were prepared by grinding the powder in an agate mortar, dispersing it in ethanol, and depositing it on a holey carbon grid. Selected area electron diffraction (SAED) patterns from 11 different crystals were obtained on a Philips CM20 transmission electron microscope equipped with the Oxford INCA system, and energy-dispersive X-ray (EDX) spectrometry was performed on those crystals to verify that the crystals were indeed the indicated phase. The cation composition of the sample as a whole was verified using EDX measurements on 68 different areas spread over 11 crystals on an FEI Osiris microscope equipped with a Super-X detector operated at 200 kV, using the L lines for La, Sr, and Ru and the K line for Ni. High-angle annular dark-field scanning TEM (HAADF-STEM) images were obtained on a probe aberration-corrected FEI Titan^3 80−300 microscope at 300 kV. The composition of the sample was supported with EDX analysis performed with a JEOL JSM5510 scanning electron microscope, equipped with the Oxford INCA system. SAED, HAADF-STEM, and quantitative EDX analysis on the pristine compounds were performed at the University of Antwerp. High-resolution TEM (HRTEM) and EDX spectra of the cycled compounds and matching TEM data of the pristine compound were obtained with a JEOL-2100F microscope equipped with the Oxford INCA system in the Institute of Catalysis and Petrochemistry in Madrid, Spain.

X-ray absorption near-edge spectroscopy (XANES) was carried out simultaneously in both the transmission and fluorescence modes on powder samples on beam line X-19A at the Brookhaven National Synchrotron Light Source using a Si(111) double-crystal monochromater.

Electrochemical Measurement. The electrochemical performance of LSNMR was investigated with an Autolab PGstat 302N potentiostat/galvanostat. A standard three-electrode glass cell and a rotating disk electrode (Pine Research Instruments) were used for the measurements. An Ag/AgCl electrode was used as the reference electrode, whereas a gold wire was used as the counter electrode.

DOI: 10.1021/acsami.9b02077
ACS Appl. Mater. Interfaces 2019, 11, 21454−21464

Unless otherwise stated, LSNMR was mixed with carbon black to improve the electrical conductivity. The mixture was placed as an ink on top of a glassy carbon working electrode. The ink was prepared by mixing 5 mg of oxide and 1 mg of carbon black (Vulcan-XC-72R) dispersed in 0.97 mL of tetrahydrofuran and 0.03 mL of Nafion, with an Ultrasonic Processor UP50H (Hielscher). The ink (10 μL) was dropped onto a glassy carbon electrode with a loading of 0.05 mg. The geometric area of the electrode was 0.196 cm^2.

For the ORR measurements, cyclic voltammograms were collected between 0.05 and 1.1 V versus RHE in an aqueous solution of 0.1 M KOH. Blank voltammograms were collected in an Ar-purged electrolyte in the ORR region (at 50 and 10 mV s^{-1}). Then, the ORR was assessed in an O_2-saturated solution at a rotation rate of 1600 rpm and 10 mV s^{-1}. Faradaic ORR currents (i_f) curves were capacitance-corrected by subtracting the curves obtained in the Ar-saturated electrolyte. The fraction of H_2O_2 generated during the ORR was evaluated with a rotating ring disk electrode (RRDE) equipped with a Pt ring set at 1.2 V. The OER kinetic curves were collected between 1.2 and 1.7 V versus RHE in the same electrolyte saturated with O_2 to ensure the O_2/H_2O equilibrium at 1.23 V. The curves were capacitance-corrected with the average of the anodic and cathodic curves. The actual production of O_2 during the OER was confirmed by following the current generated in the Pt ring RRDE at 0.4 V, the measured current accounts to the reduction of the O_2 generated during the OER (note that these experiments were measured in an Ar-purged electrolyte). OER and ORR currents were iR-corrected by the formula $E - iR_{corrected} = E_{applied} - iR$, where i is the current and R is the Ohmic electrolyte resistance ($R \approx 45\ \Omega$) as obtained from electrical impedance spectroscopy at open voltage. The ORR and OER faradaic current densities (j_f in mA cm_{geo}^{-2}) were calculated by normalizing the current to the geometric area of the electrode. Intrinsic activity and mass activity (for ORR) calculations are specified in Section S5 of the Supporting Information.

Computational Modeling. Full details of the DFT calculations and subsequent computational modeling appear in Section S7 in the Supporting Information.

RESULTS AND DISCUSSION

Crystallographic Structure. The composition determined by EDX on a transmission electron microscope was $La_{1.63(5)}Sr_{0.43(5)}Ni_{0.94(6)}Mn_{0.45(10)}Ru_{0.56(7)}O_x$, close to the nominal composition (Supporting Information). XRD data were used to establish a single phase, confirm the perovskite structure of LSNMR (Figure S1, Supporting Information), and determine the position of Ni, Mn, and Ru cations in the B/B′ sublattice. Taking into account that the general formula of double perovskites is $A_2BB'O_6$, we obtained the formula $(La_{1.5}Sr_{0.5})_A(Ni_{0.5}Mn_{0.5})_B(Ni_{0.5}Ru_{0.5})_{B'}O_6$.

TEM diffraction patterns were collected to study the crystal structure. Tilt series of different crystallites were taken to determine cell parameters and space group. Representative patterns of the main zones from these tilt series are shown in Figure 1a. All patterns were indexable with cell parameters, $a \approx b \approx \sqrt{2}a_p$, $c \approx 2a_p$, and showed reflection conditions hkl, $hk0$, and $0kl$: no conditions, $h0l$: $h + l = 2n$, $0k0$: $k = 2n$. The only space group that corresponds to these reflection conditions is $P2_1/n$. Further details on space group determination are also given in Figure S3 in the Supporting Information. The order on the B/B′ sublattice was confirmed by HAADF-STEM images (Figure 1b), of which the intensity profile shows a clear brightness difference between B and B′ columns, indicating a difference in occupation.

PND was performed for a detailed crystallographic study to determine the atomic positions, distances and angles, and occupancies of the atoms and verify the cationic location obtained by XRD, especially because the Mn neutron scattering length is extremely different from those of Ni and Ru. We used the structural parameters of La_2NiRuO_6 as the starting structural model.[30] The crystal parameters and atomic positions obtained after LSNMR structural refinement and the reliability factors are included in Table S1 (Supporting Information). The unit cell parameters determined are a = 5.5458(3) Å, b = 5.5035(3) Å, c = 7.7985(4) Å, and β = 89.95(1)°. Oxygen stoichiometry (O1, O2, and O3) was analyzed by refining the occupancy factors. We did not detect oxygen vacancies within the standard deviations. In Figure 1c, we illustrate the good agreement between observed and calculated PND patterns, and in Figure 1d, we provide a schematic view of the crystal structure.

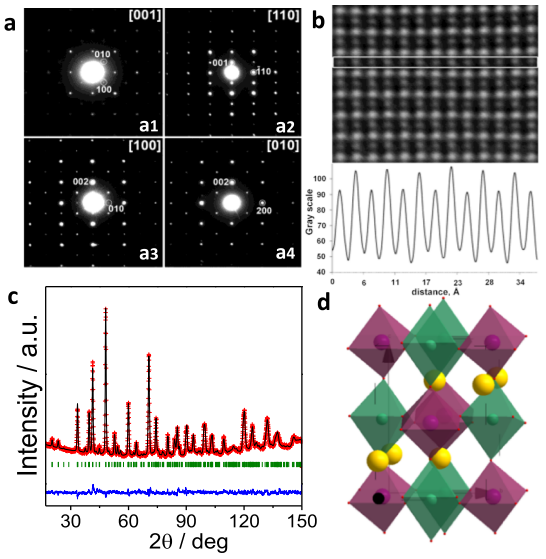

Figure 1. (a) SAED of LSNMR indexed in a perovskite cell. (b) HAADF-STEM image of LSNMR along the [010] zone. The rows of brightest dots are the columns with A cations and O, in between are rows with weaker dots, which are the B and B′ cation columns. Below the image is the intensity profile along the indicated row of B/B′ cations. (c) PND Rietveld profiles of LSNMR structure refined with the $P2_1/n$ monoclinic space group. Comparison of the observed (crosses), calculated (solid line), and difference (bottom) PND patterns. The green lines indicate the Bragg reflections. (d) Schematics of LSNMR unit cell with cell parameters a = 5.5458(3) Å, b = 5.5035(3) Å, c = 7.7985(4) Å, and β = 89.95(1)°. Purple octahedra represent $(Ni/Mn)O_6$ octahedra, green ones represent $(Ni/Ru)O_6$, and yellow spheres represent La/Sr atoms in A positions.

The atomic distances corresponding to the BO_6 and $B'O_6$ octahedra are shown in Table S2 in the Supporting Information. The main bond distances are ⟨Ni/Ru−O⟩ = 2.038(2) Å and ⟨Ni/Mn−O⟩ = 1.928(2) Å, which are larger for the $(Ni/Ru)O_6$ than the $(Ni/Mn)O_6$ octahedra; as expected from Shannon's ionic radii[31] of the transition-metal components: Ni^{2+}(VI) = 0.69 Å, Mn^{4+}(VI) = 0.53 Å, and Ru^{5+}(VI) = 0.565 Å. ⟨Ni/Ru−O⟩ = 2.038(2) Å bond distances are comparable to BO_6 distances in La_2NiRuO_6 (⟨Ni−O⟩ = 2.023 Å and ⟨Ru−O⟩ = 2.026 Å).[30] Similarly, the ⟨Ni/Mn−O⟩ = 1.928(2) distance in LSNMR is comparable with those in R_2NiMnO_6[32] and La_2NiMnO_6, where ⟨Ni/Mn−O⟩ = 1.966 Å.[33] The average of the octahedral tilt angles is calculated as $\bar{\Psi} \equiv (180 - \bar{\phi})/2 = 9.9$, where $\bar{\phi}$ is the mean ⟨B−O−B′⟩ angle. $\bar{\Psi}$ gives a measure of the degree of distortion of the perovskites. $\bar{\Psi}$ in LSNMR is smaller than in La_2CoRuO_6 ($\bar{\Psi} \approx 13.4°$)[34] or La_2NiRuO_6 ($\bar{\Psi} \approx 13°$)[30] but slightly larger than

DOI: 10.1021/acsami.9b02077
ACS Appl. Mater. Interfaces 2019, 11, 21454−21464

in $LaSrMnRuO_6$ ($\bar{\Psi} \approx 6.8°$).[35] This is because Sr^{2+} is larger than La^{3+} and the distortion of the structure is reduced when Sr is partially introduced in the A sites of the LSNMR structure.

X-ray Absorption Near-Edge Spectroscopy. XANES is a useful tool to probe constituent valence states/electronic configurations in materials where the electronic structure is being tailored to optimize specific properties.[36−39] As LSNMR contains multiple lattice sites, it provides an excellent illustration of the utility of XANES for following the charge state and balance in a complex engineered material. The near-edge features at the K-edges of 3d transition-metal compounds, M(3d), are due to transitions from the 1s to 4p states superimposed on an underlying step feature because of the onset of continuum transitions. Despite potential multiple 4p features, due to orbital orientations or superimposed 3d configurations, the systematic chemical edge shift to higher energy with increasing valence can serve as an indicator of charge states in M(3d). The spectra for the 3d sites in LSNMR are compared to the standard spectra shown in Figure 2a,b.

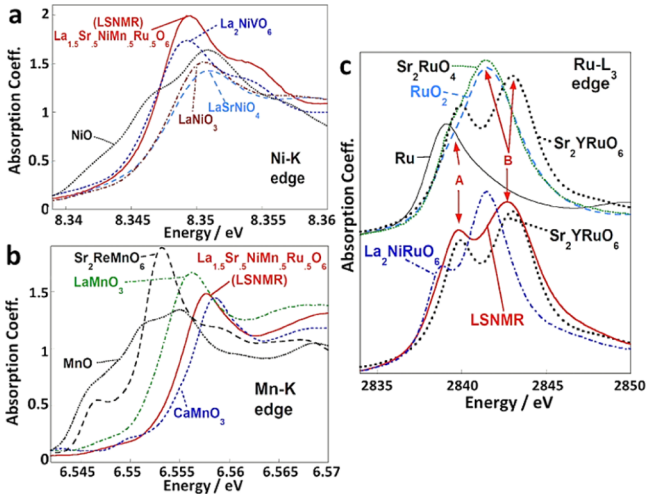

Figure 2. (a) LSNMR Ni−K main-edge spectra and $Ni^{2+}O$, $La_2Ni^{2+}VO_6$, $LaSrNi^{3+}O_4$, and $LaNi^{3+}O_3$ standards. (b) LSNMR Mn−K main-edge spectra and $Mn^{2+}O$, $Sr_2ReMn^{2+}O_6$, $LaMn^{3+}O_3$, and $CaMn^{4+}O_3$ standards. (c) Top: Ru-L_3 spectra for a series of standard compounds: metallic Ru, Ru^{4+} $4d^4$ RuO_2, and Sr_2RuO_4; and Ru^{5+} $4d^3$ Sr_2YRuO_6. Bottom: Ru-L_3 spectrum of LSNMR superimposed with $La_2NiRu^{4+}O_6$ and $Sr_2YRu^{5+}O_6$ standards. A(t_{2g}) and B(e_g) features are indicated in the figure.

The chemical shift of the Ni−K edge for LSNMR is consistent with assigning a Ni^{2+} configuration. In the Supporting Information, Figure S4a, the Ni−K pre-edge clearly supports this Ni^{2+} configuration.

In Figure 2b, the Mn K-edge is represented. The peak of LSNMR is between Mn^{3+} and Mn^{4+} standards, particularly closer to the latter. Previous studies documented a near-linear shift of the peak in the Mn−K main-edge spectra with doping-induced increasing formal valence.[36,40] Using a linear approximation, the position of the LSNMR main-edge peak is consistent with a formal valence of just under $Mn^{3.7+}$. Comparison of the LSNMR Mn−K pre-edge to those of standard compounds (see Figure S4b in the Supporting Information) also supports a Mn configuration well above Mn^{3+}.

$L_{2,3}$ near edges of M 4d (and 5d) are dominated by intense "white line" (WL) spectral features because of the transitions into empty d-final states, which reflect the d-occupancy/valence state via both the WL spectral distribution and the chemical shift. In particular, for Ru 4d compounds with octahedral ligand coordination, the d-orbitals are split into a lower lying 6-fold-degenerate t_{2g} (A-feature) and excited 4-fold-degenerate e_g states (B-feature, Figure 2c). The A-feature systematically decreases relative to B, with increasing 4d-count over the range $4d^0$−$4d^4$ (i.e., filling the t_{2g} states) (Figure S5 in the Supporting Information). For Ru^{4+} $4d^4$ standards, RuO_2 and Sr_2RuO_4, A occurs as an unresolved low-energy shoulder on the dominant B (Figure 2c). In the double perovskites Ru^{4+} $4d^4$ La_2NiRuO_6 and Ru^{5+} $4d^3$ Sr_2YRuO_6, the larger ligand field splitting leads to well-resolved A−B features. The A feature increases from Ru^{4+} to Ru^{5+}, as the t_{2g} hole count increases. Moreover, the chemical shift of the centrum of the WL to higher energy in Ru^{5+} compared to Ru^{4+} is also clear. LSNMR is superimposed with those of Ru^{4+} and Ru^{5+} standards. The high A feature intensity and chemical shift to higher energy for LSNMR clearly support ~Ru^{5+}. A small but noticeable shift to lower energy of LSNMR (relative to $Sr_2YRu^{5+}O_6$) is worth noting. The broadening of the WL features in the LSNMR spectrum is consistent with its multiple atomic site doping.

In summary, analysis of XANES data suggests that LSNMR presents a configuration of ~Ni^{2+}, ~Mn^{4+} (with a quantitative estimate of $Mn^{3.7+}$), and ~ Ru^{5+} (with the possibility of a slightly smaller value). We emphasize here that these configurations coincide with the experimentally obtained stoichiometries.

Electrochemical Characterization. Figure 3a presents the current density (j) normalized to the electrode area (0.196 cm^2) obtained in potential sweeps between 0.2−1.1 and 1.2−1.7 V (vs RHE) iR corrected (Figure S6 in the Supporting Information) in KOH at 10 mV s^{-1}. The bifunctional properties of LSNMR can be observed. LSNMR exhibits high ORR (blue branch of the curve) and OER activities (black branch of the curve). LSNMR achieves a remarkably low bifunctional index of BI = 0.83 V (defined as the potential gap between j_{ORR} = −1 mA cm^{-2}, 0.83 V, and the potential to achieve a j_{OER} = 10 mA cm^{-2}, 1.66 V). To the best of our knowledge, this value is among the best reported to date for perovskites in alkaline media, comparable to 0.83 V reported for $La_{0.58}Sr_{0.4}Co_{0.6}Fe_{0.4}O_3$/nitrogen-doped carbon nanotubes (active to ORR).[16] If we define BI as the potential difference

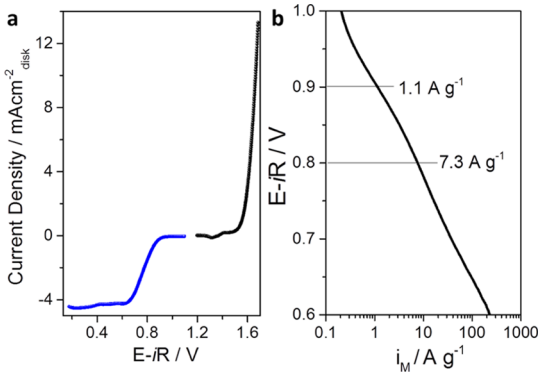

Figure 3. (a) Bifunctional ORR−OER (blue-black) current density of LSNMR in 0.1 M KOH. Relative standard deviation = 0.3 mA cm^{-2}. (b) ORR mass activity of LSNMR.

DOI: 10.1021/acsami.9b02077
ACS Appl. Mater. Interfaces 2019, 11, 21454−21464

Table 1. Activity and Durability of Some of the State-of-the-Art Bifunctional Catalysts Reported in Alkaline Media[a]

Catalyst	ORR (V) @ −1 mA cm^{-2}	OER (V) @ 10 mA cm^{-2}	BI (V)	Stability
RuO_2[57]	∼0.82	∼1.62	∼0.8	charge and discharge performance in Zn−air batteries with a stable potential retention for200 cycles
$La_{0.58}Sr_{0.4}Co_{0.2}Fe_{0.8}O_3$/N-CNT[16]	0.813	1.639	0.826	stable during and 25 h at 0.54 V (−1 mA cm^{-2}) (ORR) and 40 h at 10 mA cm^{-2} (OER)
$La_{1.5}Sr_{0.5}Ni_{0.5}Mn_{0.5}Ni_{0.5}Ru_{0.5}O_6$/C	**0.83 V**	**1.66**	**0.83**	**stable to 200 ORR and 100 OER cycles**
$La_{0.58}Sr_{0.4}Co_{0.2}Fe_{0.8}O_3/FeN_x$−C[57]	0.82	1.68	0.86	
$La_{0.6}Sr_{0.4}Co_{0.2}Fe_{0.8}O_3$/N-CNT[58]	0.72	1.60	0.88	stable during 40 h at 10 mA cm^{-2} (OER) and 25 h at 0.54 V (−1 mA cm^{-2}) (ORR)
$La_{0.7}(Ba_{0.5}Sr_{0.5})_{0.3}Co_{0.8}Fe_{0.2}O_{3-\delta}$/C[24]	0.72	1.6	0.88	stable during 100 cycles of charge−discharge at Zn−air full-cell
$LaNiO_3$/NC[2]	∼0.88	∼1.78	∼0.9	stable to cyclic voltammetry in the range of 0−1.98 V
$La_{0.3}(Ba_{0.5}Sr_{0.5})_{0.7}Co_{0.8}Fe_{0.2}O_{3-\delta}$/C[59]	∼0.7	∼1.63	∼0.93	stable to ORR during 30 000 s at 0.345 V under O_2
Hierarchical mesoporous−macroporous $La_{0.5}Sr_{0.5}CoO_{3-\delta}$[60]	∼0.7	∼1.64	∼0.94	excellent cycle stability during 50 cycles at 0.1 mA cm^{-2} in Li−O_2 battery
Co-doped $LaMnO_3$/N-CNT[61]	∼0.824	∼1.784	∼0.96	
$LaNi_{0.8}Fe_{0.2}O_3$[62]	0.694	1.714	1.02	degradation under ORR due to NiO detected on the surface. Stable to 300 OER cycles
$LaTi_{0.65}Fe_{0.35}O_{3-\delta}$ NP/N-CNR[63]	0.78	1.81	1.03	stable to charge−discharge curves at 5 A g^{-1}
$La_{0.58}Sr_{0.4}Co_{0.2}Fe_{0.8}O_{3-\delta}$ NR/N-rGO[64]	0.67	1.72	1.05	10% loss of ORR activity at 0.624 V during 18 000 s ∼15% loss of OER activity at 1.824 V during 12 000 s
$La_{0.95}FeO_{3-\delta}$[65]	0.58	1.64	1.06	
Mesoporous $La_{0.5}Sr_{0.5}CoO_{2.91}$ NW[66]	0.78	1.84	1.06	
$La_{0.6}Sr_{0.4}CoO_{3-\delta}$[67]	0.755	1.835	1.08	charge−discharge curves on Li−air batteries: stable during 50 cycles at 0.1 mA cm^{-2}
$LaMnO_{2.77}$ NP[68]	0.86	1.95	1.09	10% decrease of activity after 30 h at 0.7 V in O_2 (ORR). Stable after 10 OER cycles
$Y_2(Ru_{2-x}Y_x)O_{7-\delta}$/C[27]	0.54	1.64	1.10	
$LaNi_{0.85}Mg_{0.15}O_3$[69]	0.714	1.864	1.15	
$La_{0.8}Sr_{0.2}Mn_{0.6}Ni_{0.4}O_3$[70]	0.71	1.87	1.16	79 cycles of lifespan as cathode in a metal−air battery
$LaMnO_3$ NR/C[71]	0.705	1.885	1.18	stable during 44 000 s at 0.635 V under O_2 (ORR) 20% loss of OER activity at 1.685 V during 44 000 s
$BaTiO_{3-\delta}$/C[72]	0.72	1.90	1.18	acceptable stability for ORR and OER during 5000 s at constant potentials of 0.6 and 1.5 V, respectively
IrO_2[57]	0.38	1.70	1.32	

[a]BI between −1 and 10 mA cm^{-2}.

between 10 mA cm^{-2} (OER) and −3 mA cm^{-2} (ORR), then LSNMR-BI is 0.925 V. See Tables 1 and 2 for comparison with state-of-the-art bifunctional catalysts. For instance, the BI is lower than ∼1 V for $Ba_{0.9}Co_{0.5}Fe_{0.4}Nb_{0.1}O_3$, $LaMnO_3$, and $LaNiO_3$,[42−44] which is also among the best reported for perovskites, but surpassed by $Nd_{1.5}Ba_{1.5}CoFeMnO_{9-\delta}$ hybridized with nitrogen-doped reduced graphene oxide (BI = 0.698 V),[45] $La_{0.5}Sr_{0.5}Co_{0.8}Fe_{0.2}O_3$/nitrogen-doped carbon nanotubes (BI = 0.88),[41] $La_{0.6}Sr_{0.4}Co_{0.2}Fe_{0.8}O_3$ (BI = 0.883 V) or $La_{0.58}Sr_{0.4}Co_{0.2}Fe_{0.8}O_3$ with incorporated $Fe/N_x/C$ moieties (BI = 0.91 V).[21] It is worth to remark that the low BIs reported in refs[16,21,45] are a result of the combined contribution of the perovskite and Fe/N- and N-doped carbons, which are very active themselves for the ORR.

As observed in Figure 3a, LSNMR presents an ORR onset potential E_{onset} of 0.94 V (defined as the potential at which the current density achieves 0.1 mA cm_{disk}^{-2}), which is analogous to the most active perovskites reported for ORR to date in alkaline media, for instance, $LaNiO_3$ with 0.95 V, $LaMnO_{3+\delta}$ with ∼0.91 V, or $LaCoO_3$ with 0.85 V,[46−48] and not much lower than Pt/C (∼1.01 V) or Fe/N/C (∼1.05 V) in alkaline media.[49,50] Moreover, LSNMR records the ORR activity even at very low potentials (as low as 0.05 V), which is a remarkable observation because mixed oxides are usually not stable below ∼0.4 V.[46,51] Therefore, a proper limiting current is attained with LSNMR. The value of the half-wave potential for LSNMR (0.72 V) is worse than the values obtained for non-noble metal catalysts and platinum in alkaline media (ca. 0.87 and 0.89 V, respectively).[50] Most perovskites are not stable to low potentials, so it is complicated to achieve limiting current. Therefore, it has been established for perovskites that $E_{1/2}$ is the potential at −3 mA cm^{-2}. In that case, LSNMR ($E_{1/2}$ = 0.73 V) is superior than $Nd_{1.5}Ba_{1.5}CoFeMnO_{9-\delta}$ (0.698 V) and also than $Ba_{0.5}Sr_{0.5}Co_{0.8}Fe_{0.2}O_{3-\delta}$ (0.641 V) and $NdBaCo_2O_{5+\delta}$ (0.653 V) perovskites, only lower than $LaNiO_3$ perovskite (∼0.78 V).

The ORR kinetic current (i_k) and the mass activities are calculated. Figure 3b shows the mass activity of LSNMR with 1.1 A g^{-1} at 0.9 V and 7.3 A g^{-1} at 0.8 V. For comparison, $LaNiO_3$ was reported with a lower mass activity (0.7 A g^{-1}) at 0.9 V in the same alkaline conditions.[52] Figure S7 in the Supporting Information shows the RRDE measurement of the ORR reaction, where only 6% of the product obtained is H_2O_2.

The specific surface area of the oxide was calculated from the electrochemical surface area (Section S5, Figure S8 in the Supporting Information) and from BET (Section S6, Figure S11 in the Supporting Information). The intrinsic activity (Figure S9 in the Supporting Information) of LSNMR was estimated normalizing the obtained current by the BET value (2 m^2 g^{-1}) and the mass of oxide. From the intrinsic activity, we get that LSNMR requires a potential of 0.86 V to achieve

DOI: 10.1021/acsami.9b02077
ACS Appl. Mater. Interfaces 2019, 11, 21454−21464

Table 2. Activity and Durability of Some of the State-of-the-Art Bifunctional Catalysts Reported in Alkaline Media[a]

Catalyst	ORR (V) @ −3 mA cm^{-2}	OER (V) @ 10 mA cm^{-2}	BI (V)	Stability
$La_{0.8}Ca_{0.2}MnO_3$/AB[73] [b]	0.892	1.564	0.672	Stable 10 h of charge−discharge at 10 mA cm^{-2}in rechargeable zinc−airbatteries.
$Nd_{1.5}Ba_{1.5}CoFeMnO_{9-\delta}$/N-rGO[45]	0.889	1.587	0.698	ORR: stable 10 h at −3 mA cm^{-2}. OER: stable 10 h at 5 mA cm^{-2}
$La_{0.7}Ca_{0.3}MnO_3$/AB[73] [b]	0.873	1.593	0.720	
Ir/C[45]	0.792	1.561	0.769	
$La_{0.6}Ca_{0.4}MnO_3$/AB[73] [b]	0.85	1.633	0.783	
$La_{0.9}Ca_{0.1}MnO_3$/AB[73] [b]	0.858	1.651	0.793	
Pt/C[45]	0.894	1.695	0.801	
Pd/KB[74]	0.84	1.68	0.837	
$Pb_2Ru_2O_{6.5}$/KB[75]	0.81	∼1.65	0.84	∼30% loss of ORR activity after 1500 s at 0.7 V. ∼20% loss of OER activity after 1500 sat 1.5 V
$Ba_{0.5}Sr_{0.5}Co_{0.8}Fe_{0.2}O_{3-\delta}$/NC[76]	0.74	1.58	0.84	stable after 1000 ORR cycles and 1000 OER cycles
$PrBa_{0.85}Ca_{0.15}MnFeO_{5+\delta}$/CB[77]	0.77	1.64	0.87	loss of 5% activity after 12 h at $E_{1/2}$ (ORR). Stable after 12 h at 5 mA cm^{-2} (OER)
$La_{0.6}Sr_{0.4}Fe_{0.8}Co_{0.2}O_3$/KB[74]	0.77	1.65	0.883	stable to 2000 charge−discharge cycles at ±80 mA cm^{-2}
$Nd_{1.5}Ba_{1.5}CoFeMnO_{9-d}$[45]	0.698	1.589	0.891	
$La_{1.5}Sr_{0.5}Ni_{0.5}Mn_{0.5}Ni_{0.5}Ru_{0.5}O_6$/C	**0.73**	**1.66**	**0.925**	**stable to 200 ORR and 100 OER cycles**
$MnCoFeO_4$/N-rGO[78]	0.78	1.71	0.93	ORR stability activity decrease of 23.7% after 30 000 s of continuous operation. Loss of more than 50% OER activity after 200 cycles
RuO_2/C[78]	0.68	1.62	0.94	
$La(Co_{0.55}Mn_{0.45})_{0.99}O_{3-\delta}$ NR/N-rGO[79]	0.782	1.742	0.960	2.45% h^{-1} degradation rate on ORR at 0.385 V. 0.4 mV h^{-1} degradation rate on OER at 0.1 mA cm^{-2}
$LaCoO_3$/NC[80]	0.64	1.64	1.00	
Ru/C[81]	0.61	1.62	1.01	
$LaNi_{0.75}Fe_{0.25}O_3$/C[80]	0.67	1.68	1.01	
$LaNiO_3$/NC[23]	0.64	1.66	1.02	
$LaNiO_3$ NP/NC[23]	0.64	1.66	1.02	
MnO_x[81]	0.73	1.77	1.04	
$LaNiO_3$ NR/rGO[82]	0.628	1.705	1.077	
$La_{0.8}Sr_{0.2}MnO_3$ NR/C[83]	0.669	∼1.76	∼1.09	acceptable stability for ORR and OER during 40 000 s at constant potentials of 1.785 and 0.685 V, respectively
Co_3O_4/Co_2MnO_4[84]	0.68	1.77	1.09	loss of 6% ORR activity at 0.7 V 10 000 s in O_2. Loss of 3.2% of OER activity after 1000 cycles
$MnCoFeO_4$/C[78]	0.59	1.71	1.12	
$Mn_{1.5}Fe_{1.5}O_4$/C[78]	0.66	1.80	1.14	

[a]BI between −3 and 10 mA cm^{-2}. [b]All data are reported in alkaline electrolyte, but catalyst loading, rotation speed, scan rate, O_2 or inert saturated electrolyte, and electrolyte concentration are not consistent between data. Acetylene black (AB), carbon black (CB), Ketjenblack (KB), reduced graphene oxide(rGO), N-doped C (NC), nanorods (NR), nanoparticles (NP), nanowires (NW), nanotubes (NT). OER @ −10 mA cm^{-2}.

−0.1 mA cm_{oxide}^{-2}, being among the most active perovskites for the ORR in alkaline media.[47]

We now turn to the discussion of the OER activity of LSNMR. Figure 3a shows the OER current densities normalized by the geometric area. At 1.6 V, LSNMR reaches a current density of 3.8 mA cm_{disk}^{-2}. This value compares well with the state-of-the-art mixed oxide catalysts such as ca. 3.5 mA cm_{disk}^{-2} for $SrCo_{0.8}Fe_{0.2}O_3$ or ca. 5 mA cm_{disk}^{-2} for $BaNiO_3$.[21,53,54] On the other hand, the potential where the OER achieves a current density of 1 mA cm^2 is 1.55 V. This value is similar to that of RuO_2 and IrO_2 nanoparticles (ca. 1.55 V) for the same current density in alkaline media,[10] with the advantage that the amount of critical raw material in LSNMR is significantly lower than that for Ru and Ir metals and oxides. The potential to achieve 10 mA cm^{-2} has been suggested as the figure of merit to evaluate the OER activity of a catalyst because it is approximately the current density expected for a 10% efficient solar-to-fuel conversion device. The LSNMR catalyst records 1.65 V at such current density, similar or better than the Ni-based catalysts in alkaline media.[55] Another remarkable advantage of LSNMR is its stability under OER conditions (see below), which is exceptionally high compared to other Ru-mixed oxides.[56] We performed RRDE measurements with a Pt ring settled at 0.4 V to confirm the production of O_2 during the OER; the O_2 produced by LSNMR was reduced on the Pt ring (Figure S10).

Computational Modeling. To rationalize the high simultaneous activity of LSNMR for the OER and ORR, we modeled both reactions by means of DFT calculations; see full details in Section S7 in the Supporting Information. Briefly, if one assumes that in alkaline media the 4-electron OER pathway is[86] $OH^- \rightarrow *OH \rightarrow *OOH \rightarrow O_2$ and that the ORR proceeds in the opposite direction through the same intermediates, it is possible to calculate the reaction energies of each step based on the adsorption energies of the adsorbed intermediates *O, *OH, and *OOH (see Table S3). In turn, the overpotential for each electrode reaction (η_{OER} and η_{ORR}, see again Table S3) is calculated as the largest uphill step among those in the respective pathways. When dealing with numerous different materials, it is possible to use descriptors to go beyond the separate analysis of data and be able to capture trends in overpotentials. This is apparent in Figure 4, where the ORR and OER overpotentials are plotted as a function of a descriptor called ESSI[85,87] (see Section S7) for the three

DOI: 10.1021/acsami.9b02077
ACS Appl. Mater. Interfaces 2019, 11, 21454−21464

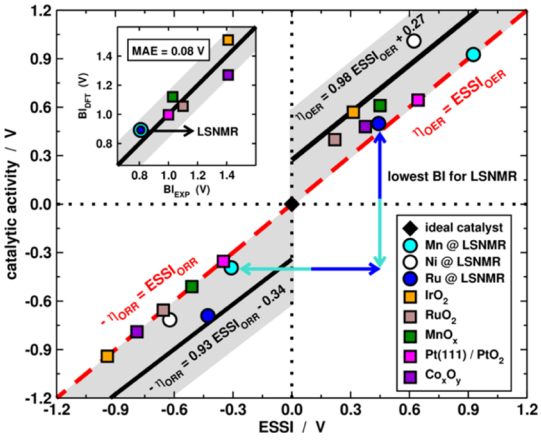

Figure 4. Calculated ORR−OER catalytic activity of various oxides (color code provided in the figure) as a function of electrochemical step symmetry index (ESSI) (see also Figure S13). For the OER, the catalytic activity is the overpotential (η_{OER}), while it is the additive inverse of the overpotential ($-\eta_{ORR}$) for the ORR. The vertical differences between the corresponding points are the BIs of the materials (marked with blue arrows for LSNMR with ORR Mn sites and OER Ru sites). The solid black lines come from ref 85. The gray area is a confidence interval of ∼85%, located approximately ±0.3 eV around those lines, that is, 1.5 times the MAE between actual DFT predictions and those of ESSI. Inset: Parity plot for DFT-calculated and experimental BIs, see full details in Section S7. The MAE between experiments and simulations is only 0.08 V and is represented by the gray shaded stripe.

transition-metal sites at LSNMR, namely, Mn, Ni, and Ru, together with other active oxides (see the data sources provided in Section S7).

In a few words, ESSI measures the energetic deviations of each material from the ideal catalyst as a result of their suboptimal adsorption energies. Such deviations are important as they are ultimately responsible for the overpotential and make it difficult to optimize electrocatalysts. As shown in Figure 4, ESSI captures the trends in overpotentials in a nearly linear fashion. More importantly, we observe that the most active sites on LSNMR surfaces for the OER are made of Ru, whereas those of Mn are most active for the ORR. Therefore, the bifunctionality of LSNMR arises from the interplay between those two ions. Compared to the other sites at LSNMR, Mn ORR sites and Ru OER sites are more symmetric, that is, their ESSI is smaller, which provides them with low overpotentials. The other combinations of active sites have larger BIs (see Table S3). Although RuO_2 is more active than LSNMR for the OER and Pt/C is more active for the ORR, the conjunction of both Mn and Ru encapsulated in LSNMR provides a lower BI.

The BI calculated for LSNMR is 0.89 V, in good agreement with the 0.83 V measured experimentally. The other oxides (and combinations of active sites in LSNMR) considered in Figure 4 display larger BIs, and we note that experiments and DFT are in good agreement in all cases, which is apparent in the inset of the figure, where a parity plot reveals a mean absolute error (MAE) between DFT and experiments of only 0.08 V, which gives confidence of the accuracy of the model and confirms the established notion that DFT is better at estimating differences in properties than properties themselves.[88,89] $\Delta ESSI = ESSI_{OER} - ESSI_{ORR}$ is shown (Figure S13 in the Supporting Information) to be a good descriptor for BI, which suggests that minimizing ΔESSI, that is, increasing the symmetry of the reaction steps for both the ORR and OER, is a suitable design principle for bifunctional catalysts.

Stability Measurements. The stability of the catalysts has been assessed by recording 200 consecutive ORR cycles between 0.1 and 1.1 V (Figure 5a) and 500 OER cycles between 1.2 and 1.7 V (Figure 5b). In Figure 5a, we illustrate how the ORR activity of LSNMR remains stable during 200 cycles. This result suggests that the compound retains its initial ORR activity. In addition, the durability of LSNMR at 0.75 V during 10 h has been assessed (see inset of Figure 5a). To evaluate the stability of the structure after cycling, we performed a *postmortem* analysis of LSNMR. Figures 6 and 7 contain representative TEM images before and after ORR and OER cycling.

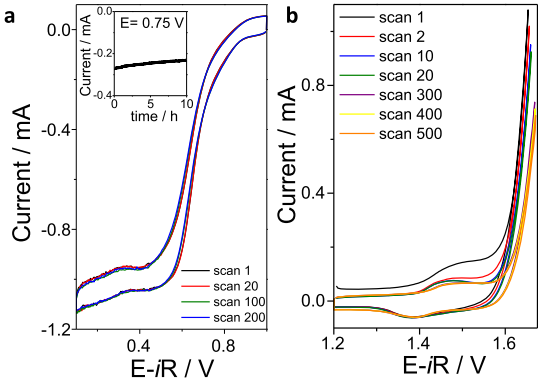

Figure 5. Durability test of LSNMR subjected to (a) up to 200 ORR cycles between 0.05 and 1 V at 50 mV s^{-1}. Inset: Chronoamperometry at 0.75 V during 10 h. (b) Up to 500 OER cycles between 1.2 and 1.7 V at 50 mV s^{-1}. The experiments were recorded in 0.1 M KOH.

Figure 6a(i−iii) illustrates the perovskite structure of the initial material (see previous section for the detailed study of the crystal structure and composition by TEM). The EDX spectrum is again shown [Figure 6a(iv)] for comparison with the EDX spectra of the cycled compounds.

Figure 6b(i) shows the TEM image of the sample after 200 ORR cycles. The HRTEM and its fast Fourier transform (FFT) can be indexed with the same cell parameters as for the pristine material, which indicates that the perovskite structure is stable upon ORR cycling [Figure 6b(ii,iii)]. The amorphous areas around the crystals are the active carbon included in the ink prepared for the electrochemical measurement (Section S8 in the Supporting Information). An EDX compositional analysis performed on several particles of the sample indicates that the crystals maintain the same composition as that of the initial oxide. This can be seen in the EDX spectrum shown in Figure 6b(iv), with only very few crystals exhibiting lower content of Sr and Ru atoms. Note that K appears in the EDX because of the electrolyte.

Figure 7 illustrates the evolution of the perovskite structure after 500 OER cycles, during which a decrease of ∼30% of the initial activity is observed. TEM results [Figure 7(i)] reveal the heterogeneous nature of the used catalyst, with nondegraded and degraded particles (1 and 2, respectively). A representative HRTEM image of the nondegraded particles is observed in Figure 7(iv), where the perovskite structure is preserved (see also FFT in the inset). EDX analysis of such particles reveals a slight decrease of Mn and Ru content, although the perovskite structure is not affected [Figure 7(ii)]. On the other hand, the

DOI: 10.1021/acsami.9b02077
ACS Appl. Mater. Interfaces 2019, 11, 21454−21464

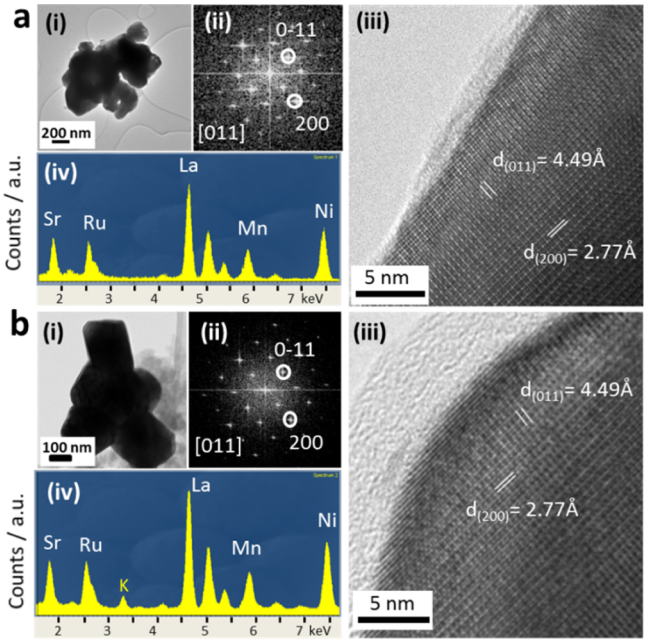

Figure 6. (a) (i) Representative TEM image of a set of particles of the initial sample. (ii) FFT of one particle along the [021] zone axis of the perovskite structure. (iii) HRTEM image and (iv) EDX spectrum. (b) (i) Representative TEM image of a set of particles after 200 ORR cycles. (ii) FFT of one particle along the [011] zone axis of the perovskite structure and its corresponding HRTEM image (iii) and EDX spectrum (iv).

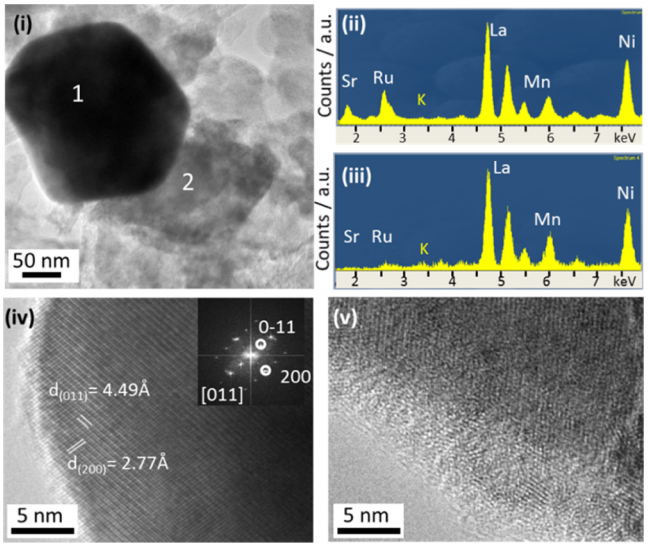

Figure 7. (i) TEM of two representative particles after 500 OER cycles. Particle 1 is nondegraded and particle 2 is degraded. (ii) EDX spectrum of a nondegraded particle. (iii) EDX spectrum of a degraded particle. (iv) HRTEM and FFT of the nondegraded particle. (v) HRTEM of the degraded particle.

HRTEM image [Figure 7(v)] of an isolated degraded particle reveals the presence of an amorphous surface layer (see also the Supporting Information, Section S8). Sr and Ru are not observed by EDX in these regions [Figure 7(iii)]. It has been previously reported for Sr–Ru-based perovskites that, after OER cycling, Sr^{2+} is dissolved in the alkaline electrolyte, and ~Ru^{5+} is oxidized into soluble species, such as RuO_4^- and its derivatives.[56,90] The presence of these particles over the entire material studied by TEM is ca. 1/4 of the total amount of particles, a finding in line with the 30% loss of OER activity observed.

The high activity and stability of this oxide for both reactions can be related to the strong redox character of the three active cations. Taking into account a formula unit, we have one Ni^{2+} that can be further oxidized to Ni^{3+}, being still stable in the perovskite. At the same time, 0.5 Mn^{4+} can be reduced to 0.5 Mn^{3+}, and 0.5 Ru^{5+} can be reduced to 0.5 Ru^{4+}. These particular valence states give the material extraordinary activity and stability to both ORR and OER reactions. In addition, the spin state is also favorable for both reactions. A global e_g filling of 1 is found in the material because we have $Ni^{2+}(d^8)$, 0.5 $Mn^{4+}(d^3)$, and 0.5 $Ru^{5+}(d^3)$. An e_g^1 filling has been recurrently reported as the ideal for perovskite catalysts for both ORR and OER.[47] In addition to this parameter, one has to consider also the covalence (hybridization) between 3d/4d orbitals of the active sites and the 2p orbitals of oxygen, which would influence the relative position of these bands with respect to the Fermi level.[91] The cations situated in the A sites of the perovskites, namely, Sr and La in this case, can also have an influence in the activity and stability of perovskite catalysts. Sr perovskites can be very active because of their configuration and structure; however, La samples are less likely to become amorphous after OER cycling in alkaline media.[3] Thus, partial replacement of Sr by La improves the stability of LSNMR.

CONCLUSIONS

LSNMR displays very high ORR and OER activity and durability in alkaline electrolytes. This bifunctional ability of LSNMR accounts to the possibility of accommodating cations in B positions with catalytic activity for different reactions, namely, Mn for the ORR and Ru for the OER. In addition, the stability of the perovskite can be increased by introducing two cations in the A sites. We demonstrate here that the versatility of perovskites to incorporate several cations within A and B sites can be further explored to design superior bifunctional catalysts.

ASSOCIATED CONTENT

Supporting Information

The Supporting Information is available free of charge on the ACS Publications website at DOI: 10.1021/acsami.9b02077.

X-ray powder diffraction; electron diffraction; PND; XANES; electrochemical performance; BET surface area; computational details; and postmortem TEM study (PDF)

AUTHOR INFORMATION

Corresponding Authors

*E-mail: m.retuerto@csic.es (M.R.).
*E-mail: srojas@icp.csic.es (S.R.).

ORCID

Federico Calle-Vallejo: 0000-0001-5147-8635
Joke Hadermann: 0000-0002-1756-2566
Martha Greenblatt: 0000-0002-1806-2766
Sergio Rojas: 0000-0002-1789-2848

Author Contributions

The manuscript was written through contributions from all authors.

DOI: 10.1021/acsami.9b02077
ACS Appl. Mater. Interfaces 2019, 11, 21454–21464

Funding

This work was supported by the ENE2016-77055-C3-3-R project from the Spanish Ministry of Economy and Competitiveness (MINECO) and PIE 201480E122 from CSIC. M.R. thanks MINECO's Juan de la Cierva program for a grant (FPDI-2013-17582). F.C.-V. thanks the Spanish MEC for a Ramón y Cajal research contract (RYC-2015-18996). M.G. acknowledges the support from NSF-DMR-1507252 grant, NJ, USA.

Notes

The authors declare no competing financial interest.

■ ACKNOWLEDGMENTS

J.H. is grateful to Maria Batuk for measuring the composition using EDX mapping and to Robert Paria Sena and Nicolas Gauquelin for their attempts to determine the valences with EELS. J.G. thanks NASI, Allahabad, India, for the award of a senior scientist fellowship.

■ REFERENCES

(1) Cheng, F.; Shen, J.; Peng, B.; Pan, Y.; Tao, Z.; Chen, J. Rapid Room-Temperature Synthesis of Nanocrystalline Spinels as Oxygen Reduction and Evolution Electrocatalysts. *Nat. Chem.* **2010**, *3*, 79−84.

(2) Chen, Z.; Yu, A.; Higgins, D.; Li, H.; Wang, H.; Chen, Z. Highly Active And Durable Core-Corona Structured Bifunctional Catalyst for Rechargeable Metal-Air Battery Application. *Nano Lett.* **2012**, *12*, 1946−1952.

(3) Gupta, S.; Kellogg, W.; Xu, H.; Liu, X.; Cho, J.; Wu, G. Bifunctional Perovskite Oxide Catalysts for Oxygen Reduction and Evolution in Alkaline Media. *Chem. Asian J.* **2016**, *11*, 10−21.

(4) Indra, A.; Menezes, P. W.; Sahraie, N. R.; Bergmann, A.; Das, C.; Tallarida, M.; Schmeisser, D.; Strasser, P.; Driess, M. Unification Of Catalytic Water Oxidation And Oxygen Reduction Reactions: Amorphous Beat Crystalline Cobalt Iron Oxides. *J. Am. Chem. Soc.* **2014**, *136*, 17530−17536.

(5) Armand, M.; Tarascon, J.-M. Building Better Batteries. *Nature* **2008**, *451*, 652−657.

(6) Lee, J.-S.; Tai Kim, S.; Cao, R.; Choi, N.-S.; Liu, M.; Lee, K. T.; Cho, J. Metal-Air Batteries with High Energy Density: Li-Air versus Zn-Air. *Adv. Energy Mater.* **2011**, *1*, 34−50.

(7) Sun, D.; Shen, Y.; Zhang, W.; Yu, L.; Yi, Z.; Yin, W.; Wang, D.; Huang, Y.; Wang, J.; Wang, D.; Goodenough, J. B. A Solution-Phase Bifunctional Catalyst for Lithium-Oxygen Batteries. *J. Am. Chem. Soc.* **2014**, *136*, 8941−8946.

(8) Jörissen, L. Bifunctional Oxygen/Air Electrodes. *J. Power Sources* **2006**, *155*, 23−32.

(9) Trasatti, S. Electrocatalysis By Oxides - Attempt At A Unifying Approach. *J. Electroanal. Chem.* **1980**, *111*, 125−131.

(10) Lee, Y.; Suntivich, J.; May, K. J.; Perry, E. E.; Shao-Horn, Y. Synthesis and Activities of Rutile IrO2 and RuO2 Nanoparticles for Oxygen Evolution in Acid and Alkaline Solutions. *J. Phys. Chem. Lett.* **2012**, *3*, 399−404.

(11) Katsounaros, I.; Cherevko, S.; Zeradjanin, A. R.; Mayrhofer, K. J. J. Oxygen Electrochemistry as a Cornerstone for Sustainable Energy Conversion. *Angew. Chem., Int. Ed.* **2014**, *53*, 102−121.

(12) Lefèvre, M.; Proietti, E.; Jaouen, F.; Dodelet, J.-P. Iron-Based Catalysts with Improved Oxygen Reduction Activity in Polymer Electrolyte Fuel Cells. *Science* **2009**, *324*, 71−74.

(13) Wu, G.; More, K. L.; Johnston, C. M.; Zelenay, P. High-Performance Electrocatalysts for Oxygen Reduction Derived from Polyaniline, Iron, and Cobalt. *Science* **2011**, *332*, 443−447.

(14) Domínguez, C.; Pérez-Alonso, F. J.; Salam, M. A.; Gómez de la Fuente, J. L.; Al-Thabaiti, S. A.; Basahel, S. N.; Peña, M. A.; Fierro, J. L. G.; Rojas, S. Effect Of Transition Metal (M: Fe, Co or Mn) for the Oxygen Reduction Reaction With Non-Precious Metal Catalysts In Acid Medium. *Int. J. Hydrogen Energy* **2014**, *39*, 5309−5318.

(15) Masa, J.; Xia, W.; Sinev, I.; Zhao, A.; Sun, Z.; Grützke, S.; Weide, P.; Muhler, M.; Schuhmann, W. MnxOy/NC and CoxOy/NC Nanoparticles Embedded in a Nitrogen-Doped Carbon Matrix for High-Performance Bifunctional Oxygen Electrodes. *Angew. Chem., Int. Ed.* **2014**, *53*, 8508−8512.

(16) Elumeeva, K.; Masa, J.; Tietz, F.; Yang, F.; Xia, W.; Muhler, M.; Schuhmann, W. A Simple Approach towards High-Performance Perovskite-Based Bifunctional Oxygen Electrocatalysts. *ChemElectroChem* **2016**, *3*, 138−143.

(17) Meng, Y.; Song, W.; Huang, H.; Ren, Z.; Chen, S.-Y.; Suib, S. L. Structure-Property Relationship of Bifunctional MnO2 Nanostructures: Highly Efficient, Ultra-Stable Electrochemical Water Oxidation and Oxygen Reduction Reaction Catalysts Identified in Alkaline Media. *J. Am. Chem. Soc.* **2014**, *136*, 11452−11464.

(18) Sakaushi, K.; Fellinger, T.-P.; Antonietti, M. Bifunctional Metal-Free Catalysis Of Mesoporous Noble Carbons For Oxygen Reduction And Evolution Reactions. *ChemSusChem* **2015**, *8*, 1156−1160.

(19) Petrie, J. R.; Cooper, V. R.; Freeland, J. W.; Meyer, T. L.; Zhang, Z.; Lutterman, D. A.; Lee, H. N. Enhanced Bifunctional Oxygen Catalysis in Strained LaNiO3 Perovskites. *J. Am. Chem. Soc.* **2016**, *138*, 2488−2491.

(20) Zhang, J.; Zhao, Z.; Xia, Z.; Dai, L. A Metal-Free Bifunctional Electrocatalyst For Oxygen Reduction And Oxygen Evolution Reactions. *Nat. Nanotechnol.* **2015**, *10*, 444−452.

(21) Chen, D.; Chen, C.; Baiyee, Z. M.; Shao, Z.; Ciucci, F. Nonstoichiometric Oxides as Low-Cost and Highly-Efficient Oxygen Reduction/Evolution Catalysts for Low-Temperature Electrochemical Devices. *Chem. Rev.* **2015**, *115*, 9869−9921.

(22) Malkhandi, S.; Yang, B.; Manohar, A. K.; Manivannan, A.; Prakash, G. K. S.; Narayanan, S. R. Electrocatalytic Properties of Nanocrystalline Calcium-Doped Lanthanum Cobalt Oxide for Bifunctional Oxygen Electrodes. *J. Phys. Chem. Lett.* **2012**, *3*, 967−972.

(23) Hardin, W. G.; Slanac, D. A.; Wang, X.; Dai, S.; Johnston, K. P.; Stevenson, K. J. Highly Active, Nonprecious Metal Perovskite Electrocatalysts for Bifunctional Metal-Air Battery Electrodes. *J. Phys. Chem. Lett.* **2013**, *4*, 1254−1259.

(24) Jung, J.-I.; Risch, M.; Park, S.; Kim, M. G.; Nam, G.; Jeong, H.-Y.; Shao-Horn, Y.; Cho, J. Optimizing Nanoparticle Perovskite For Bifunctional Oxygen Electrocatalysis. *Energy Environ. Sci.* **2016**, *9*, 176−183.

(25) Bursell, M.; Pirjamali, M.; Kiros, Y. La0.6Ca0.4CoO3, La0.1Ca0.9MnO3 and LaNiO3 as bifunctional oxygen electrodes. *Electrochim. Acta* **2002**, *47*, 1651−1660.

(26) Hamdani, M.; Singh, R. N.; Chartier, P. Co3O4 and Co- Based Spinel Oxides Bifunctional Oxygen Electrodes. *Int. J. Electrochem. Sci.* **2010**, *5*, 556−577.

(27) Park, J.; Park, M.; Nam, G.; Kim, M. G.; Cho, J. Unveiling the Catalytic Origin of Nanocrystalline Yttrium Ruthenate Pyrochlore as a Bifunctional Electrocatalyst for Zn-Air Batteries. *Nano Lett.* **2017**, *17*, 3974−3981.

(28) Rietveld, H. M. A Profile Refinement Method For Nuclear And Magnetic Structures. *J. Appl. Crystallogr.* **1969**, *2*, 65−71.

(29) Rodríguez-Carvajal, J. Recent advances in magnetic structure determination by neutron powder diffraction. *Physica B* **1993**, *192*, 55−69.

(30) Yoshii, K.; Abe, H.; Tanida, H.; Kawamura, N. Structure, magnetism and transport of La2NiRuO6. *J. Alloys Compd.* **2003**, *348*, 236−240.

(31) Shannon, R. D. Revised effective ionic radii and systematic studies of interatomic distances in halides and chalcogenides. *Acta Crystallogr.* **1976**, *32*, 751−767.

(32) Retuerto, M.; Muñoz, Á.; Martínez-Lope, M. J.; Alonso, J. A.; Mompeán, F. J.; Fernández-Díaz, M. T.; Sánchez-Benítez, J. Magnetic Interactions in the Double Perovskites R2NiMnO6 (R = Tb, Ho, Er, Tm) Investigated by Neutron Diffraction. *Inorg. Chem.* **2015**, *54*, 10890−10900.

DOI: 10.1021/acsami.9b02077
ACS Appl. Mater. Interfaces 2019, 11, 21454−21464

(33) Yang, W. Z.; Lin, X. Q.; Chen, X. M.; Chen, X. M. Structure, magnetic, and dielectric properties of La2Ni(Mn1-xTix)O6 ceramics. *J. Appl. Phys.* **2012**, *111*, 084106.
(34) Bos, J.-W. G.; Attfield, J. P. Crystal And Magnetic Structures Of The Double Perovskite La_2CoRuO_6. *J. Mater. Chem.* **2005**, *15*, 715−720.
(35) Horikubi, T.; Mori, T.; Nonobe, H.; Kamegashira, N. Synthesis and high temperature X-ray diffraction studies on the perovskite SrLaMnRuO6. *J. Alloys Compd.* **1999**, *289*, 42−47.
(36) Mandal, T. K.; Croft, M.; Hadermann, J.; Van Tendeloo, G.; Stephens, P. W.; Greenblatt, M. La2MnVO6 double perovskite: a structural, magnetic and X-ray absorption investigation. *J. Mater. Chem.* **2009**, *19*, 4382−4390.
(37) Bune, R. O.; Lobanov, M. V.; Popov, G.; Greenblatt, M.; Botez, C. E.; Stephens, P. W.; Croft, M.; Hadermann, J.; Van Tendeloo, G. Crystal Structure and Properties of Ru-Stoichiometric LaSrMnRuO6. *Chem. Mater.* **2006**, *18*, 2611−2617.
(38) Retuerto, M.; Li, M.-R.; Go, Y. B.; Ignatov, A.; Croft, M.; Ramanujachary, K. V.; Hadermann, J.; Hodges, J. P.; Herber, R. H.; Nowik, I.; Greenblatt, M. Magnetic and Structural Studies of the Multifunctional Material SrFe0.75Mo0.25O3−δ. *Acta Crystallogr.* **2012**, *51*, 12273−12280.
(39) Sahiner, A.; Croft, M.; Guha, S.; Perez, I.; Zhang, Z.; Greenblatt, M.; Metcalf, P. A.; Jahns, H.; Liang, G. Polarized XAS Studies of Ternary Nickel Oxides. *Phys. Rev. B Condens. Matter* **1995**, *51*, 5879−5886.
(40) Croft, M.; Sills, D.; Greenblatt, M.; Lee, C.; Cheong, S.-W.; Ramanujachary, K. V.; Tran, D. Systematic Mn d-configuration change in theLa1−xCaxMnO3system: A Mn K-edge XAS study. *Phys. Rev. B: Condens. Matter Mater. Phys.* **1997**, *55*, 8726−8732.
(41) Park, H. W.; Un, L. D.; Gyu, P. M.; Raihan, A.; Ho, S. M.; Nazar, L. F.; Zhongwei, C. Perovskite−Nitrogen-Doped Carbon Nanotube Composite as Bifunctional Catalysts for Rechargeable Lithium−Air Batteries. *ChemSusChem* **2015**, *8*, 1058−1065.
(42) Jin, C.; Yang, Z.; Cao, X.; Lu, F.; Yang, R. A novel bifunctional catalyst of Ba0.9Co0.5Fe0.4Nb0.1O3−δ perovskite for lithium-air battery. *Int. J. Hydrogen Energy* **2014**, *39*, 2526−2530.
(43) Davari, E.; Ivey, D. G. Bifunctional electrocatalysts for Zn-air batteries. *Sustainable Energy Fuels* **2018**, *2*, 39−67.
(44) Aijaz, A.; Masa, J.; Rösler, C.; Xia, W.; Weide, P.; Botz, A. J. R.; Fischer, R. A.; Schuhmann, W.; Muhler, M. Co@Co3 O4 Encapsulated in Carbon Nanotube-Grafted Nitrogen-Doped Carbon Polyhedra as an Advanced Bifunctional Oxygen Electrode. *Angew. Chem., Int. Ed.* **2016**, *55*, 4087−4091.
(45) Kim, N.-I.; Sa, Y. J.; Yoo, T. S.; Choi, S. R.; Afzal, R. A.; Choi, T.; Seo, Y.-S.; Lee, K.-S.; Hwang, J. Y.; Choi, W. S.; Joo, S. H.; Park, J.-Y. Oxygen-Deficient Triple Perovskites as Highly Active and Durable Bifunctional Electrocatalysts for Oxygen Electrode Reactions. *Sci. Rep.* **2018**, *4*, No. eaap9360.
(46) Retuerto, M.; Pereira, A. G.; Pérez-Alonso, F. J.; Peña, M. A.; Fierro, J. L. G.; Alonso, J. A.; Fernández-Díaz, M. T.; Pascual, L.; Rojas, S. Structural effects of LaNiO3 as electrocatalyst for the oxygen reduction reaction. *Appl. Catal., B* **2017**, *203*, 363−371.
(47) Suntivich, J.; Gasteiger, H. A.; Yabuuchi, N.; Nakanishi, H.; Goodenough, J. B.; Shao-Horn, Y. Design Principles for Oxygen-Reduction Activity on Perovskite Oxide Catalysts for Fuel Cells and Metal-Air Batteries. *Nat. Chem.* **2011**, *3*, 546−550.
(48) Suntivich, J.; Gasteiger, H. A.; Yabuuchi, N.; Shao-Horn, Y. Electrocatalytic Measurement Methodology of Oxide Catalysts Using a Thin-Film Rotating Disk Electrode. *J. Electrochem. Soc.* **2010**, *157*, B1263−B1268.
(49) Domínguez, C.; Pérez-Alonso, F. J.; Salam, M. A.; Al-Thabaiti, S. A.; Peña, M. A.; García-García, F. J.; Barrio, L.; Rojas, S. Repercussion of the Carbon Matrix for the Activity and Stability of Fe/N/C Electrocatalysts for the Oxygen Reduction Reaction. *Appl. Catal., B* **2016**, *183*, 185−196.
(50) Chung, H. T.; Won, J. H.; Zelenay, P. Active and Stable Carbon Nanotube/Nanoparticle Composite Electrocatalyst for Oxygen Reduction. *Nat. Commun.* **2013**, *4*, 1922.
(51) Pourbaix, M. *Atlas of Electrochemical Equilibria in Aqueous Solutions*; National Association of Corrosion Engineers: Houston, Texas, 1974.
(52) Karlsson, G. Reduction of oxygen on LaNiO3 in alkaline solution. *J. Power Sources* **1983**, *10*, 319−331.
(53) Lee, J. G.; Hwang, J.; Hwang, H. J.; Jeon, O. S.; Jang, J.; Kwon, O.; Lee, Y.; Han, B.; Shul, Y.-G. A New Family of Perovskite Catalysts for Oxygen-Evolution Reaction in Alkaline Media: BaNiO3 and BaNi0.83O2.5. *J. Am. Chem. Soc.* **2016**, *138*, 3541−3547.
(54) Retuerto, M.; Calle-Vallejo, F.; Pascual, L.; Ferrer, P.; García, Á.; Torrero, J.; Gianolio, D.; Fierro, J. L. G.; Peña, M. A.; Alonso, J. A.; Rojas, S. Role of Lattice Oxygen Content and Ni Geometry in the Oxygen Evolution Activity of the Ba-Ni-O system. *J. Power Sources* **2018**, *404*, 56−63.
(55) McCrory, C. C. L.; Jung, S.; Peters, J. C.; Jaramillo, T. F. Benchmarking Heterogeneous Electrocatalysts for the Oxygen Evolution Reaction. *J. Am. Chem. Soc.* **2013**, *135*, 16977−16987.
(56) Kim, B.-J.; Abbott, D. F.; Cheng, X.; Fabbri, E.; Nachtegaal, M.; Bozza, F.; Castelli, I. E.; Lebedev, D.; Schäublin, R.; Copéret, C.; Graule, T.; Marzari, N.; Schmidt, T. J. Unraveling Thermodynamics, Stability, and Oxygen Evolution Activity of Strontium Ruthenium Perovskite Oxide. *ACS Catal.* **2017**, *7*, 3245−3256.
(57) Rincón, R. A.; Masa, J.; Mehrpour, S.; Tietz, F.; Schuhmann, W. Activation of oxygen evolving perovskites for oxygen reduction by functionalization with Fe-Nx/C groups. *Chem. Commun.* **2014**, *50*, 14760−14762.
(58) Elumeeva, K.; Masa, J.; Sierau, J.; Tietz, F.; Muhler, M.; Schuhmann, W. Perovskite-Based Bifunctional Electrocatalysts for Oxygen Evolution and Oxygen Reduction in Alkaline Electrolytes. *Electrochim. Acta* **2016**, *208*, 25−32.
(59) Jung, J.-I.; Jeong, H. Y.; Lee, J.-S.; Kim, M. G.; Cho, J. A Bifunctional Perovskite Catalyst for Oxygen Reduction and Evolution. *Angew Chem. Int. Ed.* **2014**, *53*, 4582−4586.
(60) Liu, G.; Chen, H.; Xia, L.; Wang, S.; Ding, L.-X.; Li, D.; Xiao, K.; Dai, S.; Wang, H. Hierarchical Mesoporous/Macroporous Perovskite La0.5Sr0.5CoO3-x Nanotubes: A Bifunctional Catalyst with Enhanced Activity and Cycle Stability for Rechargeable Lithium Oxygen Batteries. *ACS Appl. Mater. Interfaces* **2015**, *7*, 22478−22486.
(61) Lee, D. U.; Park, M. G.; Park, H. W.; Seo, M. H.; Ismayilov, V.; Ahmed, R.; Chen, Z. Highly active Co-doped LaMnO 3 perovskite oxide and N-doped carbon nanotube hybrid bi-functional catalyst for rechargeable zinc-air batteries. *Electrochem. Commun.* **2015**, *60*, 38−41.
(62) Zhang, D.; Song, Y.; Du, Z.; Wang, L.; Li, Y.; Goodenough, J. B. Active LaNi1−xFexO3 bifunctional catalysts for air cathodes in alkaline media. *J. Mater. Chem. A* **2015**, *3*, 9421−9426.
(63) Prabu, M.; Ramakrishnan, P.; Ganesan, P.; Manthiram, A.; Shanmugam, S. LaTi 0.65 Fe 0.35 O 3−δ nanoparticle-decorated nitrogen-doped carbon nanorods as an advanced hierarchical air electrode for rechargeable metal-air batteries. *Nano Energy* **2015**, *15*, 92−103.
(64) Park, H. W.; Lee, D. U.; Zamani, P.; Seo, M. H.; Nazar, L. F.; Chen, Z. Electrospun Porous Nanorod Perovskite Oxide/Nitrogen-Doped Graphene Composite as a Bi-Functional Catalyst for Metal Air Batteries. *Nano Energy* **2014**, *10*, 192−200.
(65) Zhu, Y.; Zhou, W.; Yu, J.; Chen, Y.; Liu, M.; Shao, Z. Enhancing Electrocatalytic Activity of Perovskite Oxides by Tuning Cation Deficiency for Oxygen Reduction and Evolution Reactions. *Chem. Mater.* **2016**, *28*, 1691−1697.
(66) Zhao, Y.; Xu, L.; Mai, L.; Han, C.; An, Q.; Xu, X.; Liu, X.; Zhang, Q. Hierarchical mesoporous perovskite La0.5Sr0.5CoO2.91 nanowires with ultrahigh capacity for Li-air batteries. *Proc. Natl. Acad. Sci. U.S.A.* **2012**, *109*, 19569−19574.
(67) Oh, M. Y.; Jeon, J. S.; Lee, J. J.; Kim, P.; Nahm, K. S. The bifunctional electrocatalytic activity of perovskite La0.6Sr0.4CoO3−δ for oxygen reduction and evolution reactions. *RSC Adv.* **2015**, *5*, 19190−19198.

DOI: 10.1021/acsami.9b02077
ACS Appl. Mater. Interfaces 2019, 11, 21454−21464

(68) Du, J.; Zhang, T.; Cheng, F.; Chu, W.; Wu, Z.; Chen, J. Nonstoichiometric Perovskite CaMnO3−δ for Oxygen Electrocatalysis with High Activity. *Inorg. Chem.* **2014**, *53*, 9106−9114.
(69) Du, Z.; Yang, P.; Wang, L.; Lu, Y.; Goodenough, J. B.; Zhang, J.; Zhang, D. Electrocatalytic performances of LaNi1−xMgxO3 perovskite oxides as bi-functional catalysts for lithium air batteries. *J. Power Sources* **2014**, *265*, 91−96.
(70) Wang, Z.; You, Y.; Yuan, J.; Yin, Y.-X.; Li, Y.-T.; Xin, S.; Zhang, D. Nickel-Doped La0.8Sr0.2Mn1-xNixO3 Nanoparticles Containing Abundant Oxygen Vacancies as an Optimized Bifunctional Catalyst for Oxygen Cathode in Rechargeable Lithium-Air Batteries. *ACS Appl. Mater. Interfaces* **2016**, *8*, 6520−6528.
(71) Xu, Y.; Tsou, A.; Fu, Y.; Wang, J.; Tian, J.-H.; Yang, R. Carbon-Coated Perovskite BaMnO3 Porous Nanorods with Enhanced Electrocatalytic Properties for Oxygen Reduction and Oxygen Evolution. *Electrochim. Acta* **2015**, *174*, 551−556.
(72) Chen, C.-F.; King, G.; Dickerson, R. M.; Papin, P. A.; Gupta, S.; Kellogg, W. R.; Wu, G. Oxygen-deficient BaTiO 3−x perovskite as an efficient bifunctional oxygen electrocatalyst. *Nano Energy* **2015**, *13*, 423−432.
(73) Li, G.; Mezaal, M. A.; Zhang, R.; Zhang, K.; Liu, W.; Lei, L. Electrochemical Evaluation of $La_{1-x}Ca_xMnO_3$ in Zinc-air Batteries. *Int. J. Electrochem. Sci.* **2015**, *10*, 8412−8422.
(74) Alegre, C.; Modica, E.; Aricò, A. S.; Baglio, V. Bifunctional Oxygen Electrode Based on a Perovskite/Carbon Composite for Electrochemical Devices. *J. Electroanal. Chem.* **2018**, *808*, 412−419.
(75) Park, J.; Risch, M.; Nam, G.; Park, M.; Shin, T. J.; Park, S.; Kim, M. G.; Shao-Horn, Y.; Cho, J. Single crystalline pyrochlore nanoparticles with metallic conduction as efficient bi-functional oxygen electrocatalysts for Zn-air batteries. *Energy Environ. Sci.* **2017**, *10*, 129−136.
(76) Wang, J.; Zhao, H.; Gao, Y.; Chen, D.; Chen, C.; Saccoccio, M.; Ciucci, F. Ba0.5Sr0.5Co0.8Fe0.2O3−δ on N-doped mesoporous carbon derived from organic waste as a bi-functional oxygen catalyst. *Int. J. Hydrogen Energy* **2016**, *41*, 10744−10754.
(77) Hua, B.; Sun, Y.-F.; Li, M.; Yan, N.; Chen, J.; Zhang, Y.-Q.; Zeng, Y.; Shalchi Amirkhiz, B.; Luo, J.-L. Stabilizing Double Perovskite For Effective Bifunctional Oxygen Electrocatalysis in Alkaline Conditions. *Chem. Mater.* **2017**, *29*, 6228−6237.
(78) Zhan, Y.; Xu, C.; Lu, M.; Liu, Z.; Lee, J. Y. Mn and Co co-substituted Fe3O4nanoparticles on nitrogen-doped reduced graphene oxide for oxygen electrocatalysis in alkaline solution. *J. Mater. Chem. A* **2014**, *2*, 16217−16223.
(79) Ge, X.; Goh, F. W. T.; Li, B.; Hor, T. S. A.; Zhang, J.; Xiao, P.; Wang, X.; Zong, Y.; Liu, Z. Efficient and durable oxygen reduction and evolution of a hydrothermally synthesized La(Co0.55Mn0.45)-0.99O3−δ nanorod/graphene hybrid in alkaline media. *Nanoscale* **2015**, *7*, 9046−9054.
(80) Hardin, W. G.; Mefford, J. T.; Slanac, D. A.; Patel, B. B.; Wang, X.; Dai, S.; Zhao, X.; Ruoff, R. S.; Johnston, K. P.; Stevenson, K. J. Tuning the Electrocatalytic Activity of Perovskites through Active Site Variation and Support Interactions. *Chem. Mater.* **2014**, *26*, 3368−3376.
(81) Gorlin, Y.; Jaramillo, T. F. A Bifunctional Nonprecious Metal Catalyst for Oxygen Reduction and Water Oxidation. *J. Am. Chem. Soc.* **2010**, *132*, 13612−13614.
(82) Hu, J.; Liu, Q.; Shi, Z.; Zhang, L.; Huang, H. LaNiO3-nanorod/graphene composite as an efficient bi-functional catalyst for zinc-air batteries. *RSC Adv.* **2016**, *6*, 86386−86394.
(83) Lu, F.; Wang, Y.; Jin, C.; Li, F.; Yang, R.; Chen, F. Microporous La0.8Sr0.2MnO3 perovskite nanorods as efficient electrocatalysts for lithium-air battery. *J. Power Sources* **2015**, *293*, 726−733.
(84) Wang, D.; Chen, X.; Evans, D. G.; Yang, W. Well-dispersed Co3O4/Co2MnO4 nanocomposites as a synergistic bifunctional catalyst for oxygen reduction and oxygen evolution reactions. *Nanoscale* **2013**, *5*, 5312−5315.
(85) Govindarajan, N.; García-Lastra, J. M.; Meijer, E. J.; Calle-Vallejo, F. Does the Breaking of Adsorption-Energy Scaling Relations Guarantee Enhanced Electrocatalysis? *Curr. Opin. Electrochem.* **2018**, *8*, 110−117.
(86) Tripkovic, V.; Heine, A. H.; Juan, M.; Tejs, V. Comparative DFT+U and HSE Study of the Oxygen Evolution Electrocatalysis on Perovskite Oxides. *J. Phys. Chem. C* **2018**, *122*, 1135−1147.
(87) Man, I. C.; Su, H. Y.; Calle-Vallejo, F.; Hansen, H. A.; Martínez, J. I.; Inoglu, N. G.; Kitchin, J.; Jaramillo, T. F.; Nørskov, J. K.; Rossmeisl, J. Universality in Oxygen Evolution Electrocatalysis on Oxide Surfaces. *ChemCatChem* **2011**, *3*, 1159−1165.
(88) Krishnamurthy, D.; Sumaria, V.; Viswanathan, V. Maximal Predictability Approach for Identifying the Right Descriptors for Electrocatalytic Reactions. *J. Phys. Chem. Lett.* **2018**, *9*, 588−595.
(89) Medford, A. J.; Wellendorff, J.; Vojvodic, A.; Studt, F.; Abild-Pedersen, F.; Jacobsen, K. W.; Bligaard, T.; Norskov, J. K. Assessing the Reliability of Calculated Catalytic Ammonia Synthesis Rates. *Science* **2014**, *345*, 197−200.
(90) Chang, S. H.; Danilovic, N.; Chang, K. C.; Subbaraman, R.; Paulikas, A. P.; Fong, D. D.; Highland, M. J.; Baldo, P. M.; Stamenkovic, V. R.; Freeland, J. W.; Eastman, J. A.; Markovic, N. M. Functional links between stability and reactivity of Strontium Ruthenate Single Crystals During Oxygen Evolution. *Nat. Commun.* **2014**, *5*, 4191.
(91) Hong, W. T.; Risch, M.; Stoerzinger, K. A.; Grimaud, A.; Suntivich, J.; Shao-Horn, Y. Toward the Rational Design of Non-Precious Transition Metal Oxides for Oxygen Electrocatalysis. *Energy Environ. Sci.* **2015**, *8*, 1404−1427.

DOI: 10.1021/acsami.9b02077
ACS Appl. Mater. Interfaces 2019, 11, 21454−21464

Supporting Information

$La_{1.5}Sr_{0.5}NiMn_{0.5}Ru_{0.5}O_6$ Double Perovskite with Enhanced ORR/OER Bifunctional Catalytic Activity

Maria Retuerto[1*], Federico Calle-Vallejo[2], Laura Pascual[3], Gunnar Lumbeeck[4], María Teresa Fernandez-Diaz[5], Mark Croft[6], Jagannatha Gopalakrishnan[7], Miguel A. Peña[1], Joke Hadermann[4], Martha Greenblatt[8], Sergio Rojas[1*]

[1] Grupo de Energía y Química Sostenibles, Instituto de Catálisis y Petroleoquímica, CSIC. C/ Marie Curie 2, L10. 28049, Madrid, Spain.
[2] Departament de Ciència de Materials i Química Fisica & Institut de Química Teòrica i Computacional (IQTCUB), Universitat de Barcelona, Martí i Franqués 1, 08028 Barcelona, Spain
[3] Instituto de Catálisis y Petroleoquímica, CSIC. C/ Marie Curie 2, L10. 28049, Madrid, Spain.
[4] EMAT, University of Antwerp, Groenenborgerlaan 171, 2020 Antwerp, Belgium
5 Institut Laue-Langevin, BP156X, Grenoble, F-38042, France.
6 Department of Physics, Rutgers, The State University of New Jersey, 610 Taylor Road, Piscataway, New Jersey, 08854, USA
7 Solid State and Structural Chemistry Unit, Indian Institute of Science, Bangalore 560 012, India.
8 Department of Chemistry and Chemical Biology, Rutgers, The State University of New Jersey, 610 Taylor Road, Piscataway, New Jersey, 08854, USA

Corresponding Authors
* srojas@icp.csic.es, m.retuerto@csic.es

Table of Contents

S1. X-Ray Powder Diffraction

Figure S1 shows the Rietveld refinement of the structure of $La_{1.5}Sr_{0.5}NiMn_{0.5}Ru_{0.5}O_6$ (LSNMR) in P$2_1/n$ space group by x-ray diffraction.

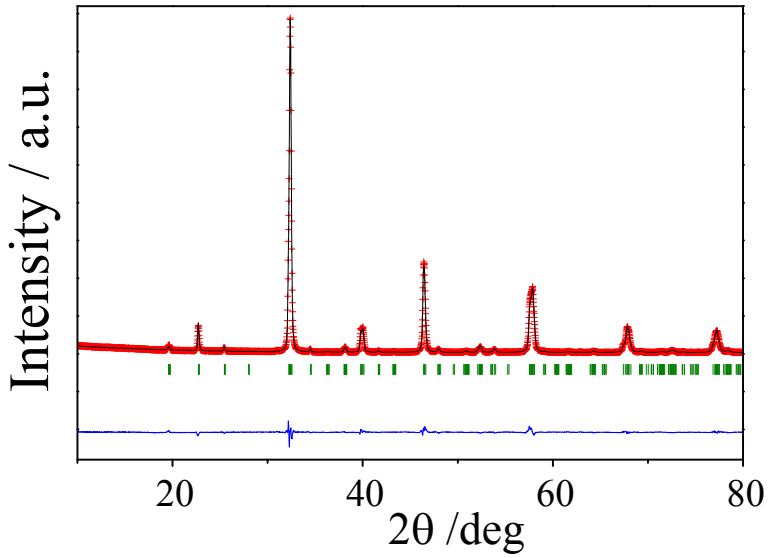

Figure S1. XRD Rietveld profiles of the structure of $La_{1.5}Sr_{0.5}NiMn_{0.5}Ru_{0.5}O_6$, LSNMR, refined with the P$2_1/n$ monoclinic space group. Crosses are the observed pattern, the black full line is the calculated one and the bottom blue line is the difference between both. The green lines indicate the Bragg reflections of the selected space group.

S2. Electron Diffraction

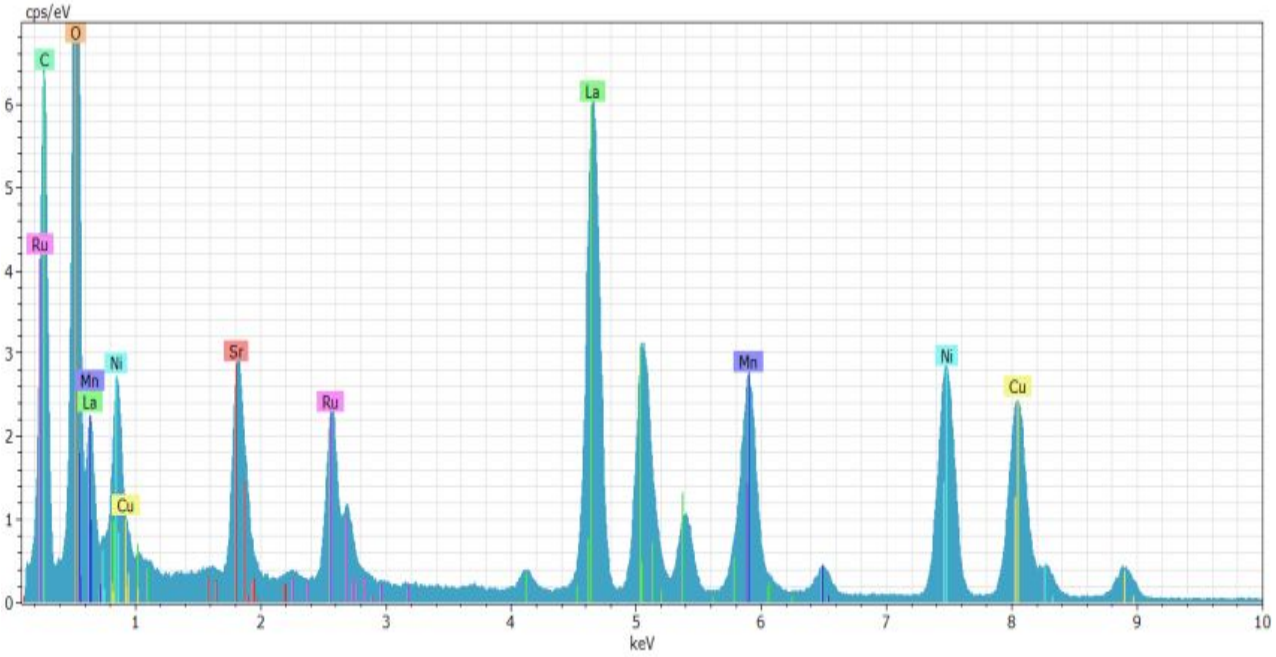

Figure S2. Representative EDX spectrum of LSNMR to illustrate the composition obtained.

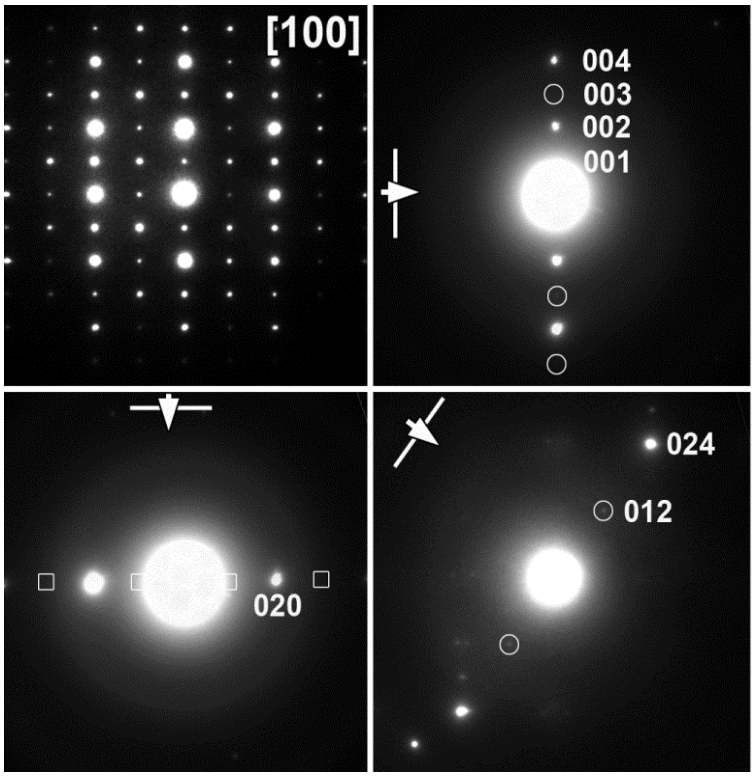

Figure S3. Selected Area Electron Diffraction (SAED) of LSNMR indexed in a perovskite cell.

As shown in Figure S3, by tilting around the relevant rows of reflections, the 0k0: k = 2n+1 reflections (indicated by squares) are due to double diffraction, since they disappear when removing the possible double diffraction paths, while 00l: l = 2n+1 (indicated by circles in the top right pattern) are not due to double diffraction. We investigated whether the [100] patterns could actually be twinned patterns of [100] with 0kl: k = 2n and [010] with h0l: h+l = 2n, with the 0kl: k = 2n+1, l = 2n being due to double diffraction only. This is necessary since this would exactly correspond to P*bnm* (or in the conventional setting for perovskites P*nma* with $a \approx \sqrt{2}a_p$, $b \approx 2a_p$, $c \approx \sqrt{2}a_p$), which has the same octahedral tilt pattern as $P2_1/n$ but without cation order. The tilt around the 0kl: l = 2k row of reflections, shown also in Figure S3 (indicated by circles in the bottom right pattern), show that these reflections remain present even when all double diffraction paths to these reflections are eliminated. This proves that these reflections are not due to double diffraction on top of a twinned pattern, but that there is indeed no reflection condition for 0kl reflections. Therefore, only $P2_1/n$ is in agreement with the experimental electron diffraction results.

S3. Powder Neutron Diffraction

Table S1. Atomic parameters after the refinement of the crystallographic structure of $La_{1.5}Sr_{0.5}NiMn_{0.5}Ru_{0.5}O_6$ from high resolution PND data at T = 295 K. Space group $P2_1/n$. Lattice parameters: a = 5.5458(3) Å, b = 5.5035(3) Å, c = 7.7985(4) Å, ß = 89.95(1)º and V = 238.02(2) Å^3. Discrepancy factors: R_p = 2.38%, R_{exp} = 2.17%, R_{wp} = 3.07% and R_{Bragg} = 5.57%, χ^2 = 1.99.

Atom	**Site**	**x**	**y**	**z**	**f_{occ}**	**B(Å^2)**
La/Sr	*4e*	0.0032(8)	0.0213(5)	0.2518(9)	0.75/0.25	0.12(4)
Ni/Ru	*2a*	1/2	0	1/2	0.5/0.5	0.17(5)
Ni/Mn	*2b*	1/2	0	0	0.5/0.5	0.17(5)
O1	*4e*	0.2937(9)	0.2796(11)	0.0322(9)	1.000	0.01(4)
O2	*4e*	0.2429(9)	0.7634(9)	0.0320(8)	1.000	0.01(4)
O3	*4e*	-0.0690(7)	0.4909(8)	0.26120(9)	1.000	0.01(4)

Table S2. Atomic distances (Å) for Ni/RuO_6 and Ni/MnO_6 octahedra and selected bond angles (º) at 295 K.

Description	Bond distance
Ni/Ru – O1 (x2)	2.046(5)
Ni/Ru – O2 (x2)	1.995(5)
Ni/Ru – O3 (x2)	2.073(6)
< Ni/Ru – O>	2.038(2)
Ni/Mn – O1 (x2)	1.934(6)
Ni/Mn – O2 (x2)	1.947(5)
Ni/Mn – O3 (x2)	1.902(6)
< Ni/Mn – O >	1.928(2)
Description	Angle
(Ru/Ni-O1-Mn/Ni)	157.9(2)
(Ru/Ni-O2-Mn/Ni)	164.7(2)
(Ru/Ni-O3-Mn/Ni)	157.6(3)

S4. X-ray absorption near edge spectroscopy (XANES)

S4.1. Ni-K and Mn-K pre-edges

The 3d row transition metal pre-edge features are due to quadrupole-allowed transitions into final *d*-states or into hybridization-allowed dipole transitions into *d*/ligand-*p* states. Those are shifted below the main edge by the final state *d*-electron/core-hole Coulomb interaction. The spectral shape, intensity, and chemical shift of the pre-edge features can also be used as valence indicators.[1-3] In the case of the Ni-K pre-edge, doping studies have shown a systematic increase in pre-edge feature intensity and chemical shift for Ni valences in the 2+ to 3.3+ range.[1] In Figure S4a, the Ni-K pre-edge of LSNMR exhibits a low chemical shift and spectral area (close to $La_2Ni^{2+}VO_6$). Thus, both the Ni-K main edge and pre-edge results support Ni^{2+} configuration in LSNMR.

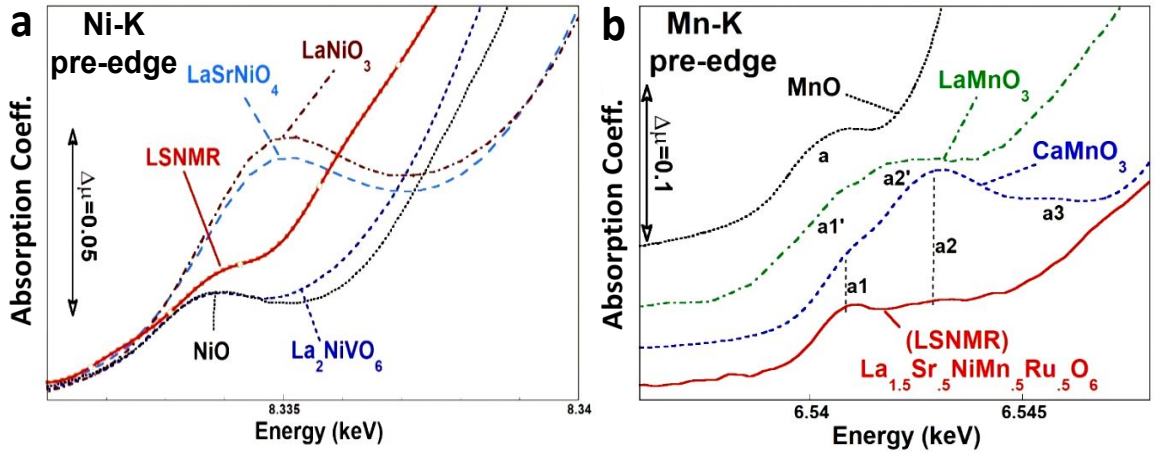

Figure S4(a). Ni-K pre-edge spectra for LSNMR and the standard compounds: ~Ni^{2+} standards NiO and La_2NiVO_6; and ~Ni^{3+} standards $LaNiO_3$ and $LaSrNiO_4$. **(b)** Mn-K pre-edge spectra for LSNMR and the standard compounds: ~Mn^{2+}, MnO; ~Mn^{3+}, $LaMnO_3$; and ~Mn^{4+}, $CaMnO_3$. Note the standard spectra have been displaced vertically for clarity and nominal pre-edge features are identified.

Figure S4b compares the Mn-K pre-edge of LSNMR to those of standard Mn compounds. It should be noted that a1-a2 features for the Mn^{4+} standard are shifted up in energy relative to the a1'-a2' features in the Mn^{3+} standard. The a1-a2 features for LSNMR are similar in energy (albeit less intense) to the Mn^{4+} standard. Thus the Mn-K pre-edge feature structure and intensity only supports a Mn valence well above 3+.

S4.2. 4d-L_3 edges

Figure S5 shows the systematic M(4*d*)-L_3 edge variation with 4*d*-count for octahedral ligand coordination. The $L_{2,3}$-edges of transition metals are dominated by intense "white line" (WL) spectral features at the edge onsets.[3-6] These WL-features are due to transitions

into empty *d* final states and can be used as a probe of the *d* occupancy through both their spectral distribution and chemical shift. In the case of 4*d* transition metal compounds, with octahedral ligand coordination, the 4*d*-orbitals are split into a lower lying 6-fold-degenerate t_{2g} and excited 4-fold-degenerate e_g states. To first-order this ligand field splitting is reflected in a splitting of the 4d-$L_{2,3}$-edge WL-features in such compounds into a bimodal A(t_{2g} related)/B(e_g related) structure (see the A and B features and Figure S5). This splitting is illustrated in Figure S5 for the L_3 edges of 4d-row perovskite related compounds.[3-6] It should be noted that the intensity of the A(t_{2g} related) feature systematically decreases, relative to the B(e_g related) feature, as the 4d configuration increases from $4d^0$ to $4d^4$ (i.e. as the t_{2g} hole count decreases from 6 to 2). It is worth noting that while the ligand field split levels and systematic 4d-occupation trends are apparent in such compounds, multiplet and spin orbit interaction effects can also be discerned in 4d-row compounds.[5]

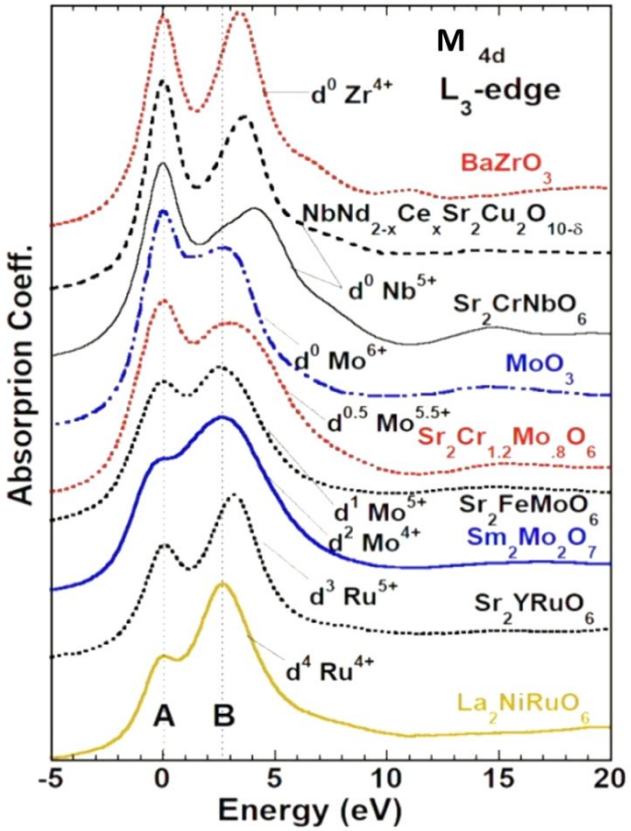

Figure S5. The M-L_3 edges of a series of T_{4d} compounds (with octahedral O-ligand symmetry), T_{4d} = Zr, Nb, Mo, and Ru, with d-occupancies varying from d^0 to d^4. For comparison, the spectra have been nominally aligned to the A-(t_{2g} related) feature. Note the systematic decrease in the A-feature intensity, relative to the B-(e_g related) feature as the d-count increases (i.e. as the d final state hole count decreases).

The first conclusion of the XANES is that it supports the LSNMR formula with the nominal formal valences of Ni^{2+}-Mn^{4+}-Ru^{5+}, with the caveat that integral valence states in the solid-state environment are a substantial oversimplification. A configuration of the Ni^{2+} is strongly supported. A configuration of close to Mn^{4+} is evidenced with a quantitative estimate of $Mn^{3.7+}$ being motivated by main-edge peak position. A configuration of close to Ru^{5+} is evidenced, but with the possibility of a somewhat smaller value based upon the chemical shift.

The main-edge evidence for the more precise estimate of $Mn^{3.7+}$ does have an empirical basis and should be noted. In this regard it is worth noting that the weighted average of the SEM and TEM stoichiometries $[La_{0.80(3)}Sr_{0.24(3)}Ni_{0.5(1)}Mn_{0.27(3)}Ru_{0.22(8)}O_x]$ would almost precisely agree with Ni^{2+} - $Mn^{3.7+}$ - Ru^{5+} if x = 3. In view of the uncertainties, this stoichiometry/Mn-valence is likely fortuitous, but it emphasizes that the question of a possible Mn-valence somewhat lower than 4+ in LSNMR must remain open. The evidence for a Ru-valence slightly less than 5+ is less strong, but should also be considered an open question.

S5. Electrochemical Performance

S5. 1. Electrochemical impedance spectroscopy (EIS)

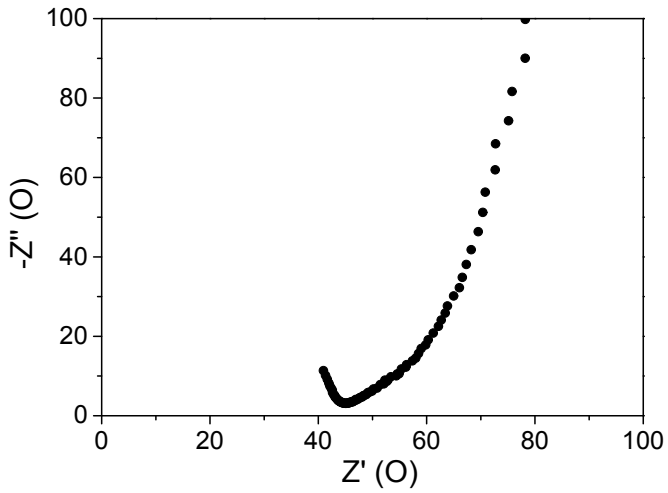

Figure S6. Nyquist plot of LSNMR from an electrochemical impedance spectroscopy experiment at open voltage.

S5.2. RRDE measurement to determine the production of H_2O_2 during the ORR.

The ORR can proceed via 4 electrons ($O_2 \rightarrow H_2O$) or 2 electrons ($O_2 \rightarrow H_2O_2$) and the relative production of H_2O_2 was assessed using a RRDE with a Pt ring at 1.2 V during the ORR reaction. At 1.2 V, the H_2O_2 eventually formed during the ORR, produces O_2 at the Pt ring, giving oxidizing currents. The H_2O_2 fraction formed is calculated from the formula:

$$X_{H_2O_2} = \frac{\frac{2i_R}{N}}{i_D + \frac{i_R}{N}} \quad \text{(S1)}$$

where i_D is the current obtained at the disk and i_R is the current obtained at the Pt ring. N is the ring's efficiency, set at 26 %. The number of exchanged electrons is then calculated from:

$$ne = 4 - \left(\frac{\%H_2O_2}{50\%}\right) \quad \text{(S2)}$$

The RRDE measurement (Figure S7) shows that 6% of the product obtained during ORR is H_2O_2.

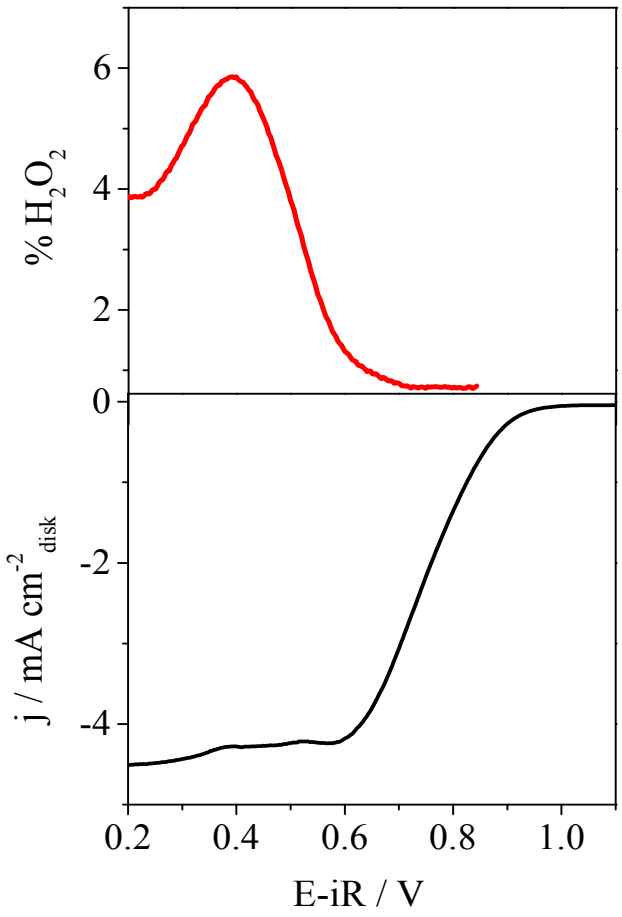

Figure S7. RRDE ORR measurement with the Pt ring settled at 1.2 V.

S5.3. ECSA

The electrochemically active surface area (ECSA) was calculated by the double-layer capacitance of LSNMR without active carbon. We performed cyclic voltammograms at different velocities close to the "*open circuit potential*" in Ar, where it is suppose that the measured currents are due to double-layer charging. ECSA was recorded at 200, 100, 50, 20 and 10 mV/s between 0.78 and 0.98 V *vs.* RHE (Figure S8). The double-layer charging current would be equal to the product of the scan rate (ν) and the double-layer capacitance (C_{dl}) as $i_c = \nu C_{dl}$. If i_c is plotted as a function of ν, then the slope will be C_{dl}, and ECSA will be ECSA= C_{dl}/ C_S; where C_S is the specific capacitance of an atomically flat planar surface of the material per unit area under identical electrolyte conditions. Since this value is not well established for oxides we used 0.06 mF/cm^2, used in several references for 0.1M KOH.[7] The ECSA obtained was 2 cm^2.

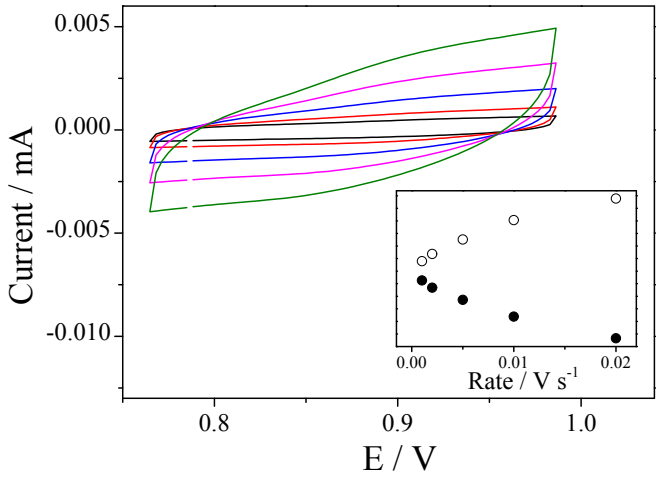

Figure S8. ECSA calculations of LSNMR.

S5.4. Intrinsic Activity

Intrinsic activities (i_s in $mAcm^{-2}_{oxide}$) were calculated by normalizing i_f to the actual specific surface area of the oxide deposited on the electrode with the following equation:

$$i_s = \frac{i_f}{(g_{oxide} x BET_{oxide})} \quad \text{(S3)}$$

where BET_{oxide} is the specific surface area of LSNMR, namely 2 m^2/g, obtained from the BET measurements.

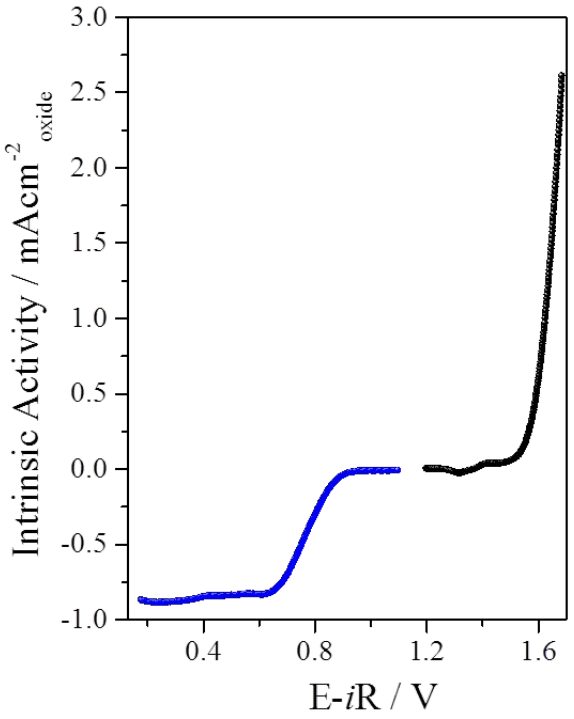

Figure S9. ORR and OER Intrinsic Activities of LSNMR.

S5.5. ORR Kinetic current and Mass Activity.

ORR kinetic current (i_k) are calculated from the Koutecky–Levich equation:

$$i_k = -\frac{i_F \times i_{lim}}{i_F - i_{lim}} \quad \text{(S4)}$$

where i_F is the Faradaic current and i_{lim} is the limiting current. Using the kinetic current we calculate the mass activity of LSNMR (Figure 3b of the main text):

$$i_m = -\frac{i_k}{g_{oxide}} \quad \text{(S5)}$$

.6. RRDE measurement to determine the production of O_2 during the OER.

We performed RRDE measurement during the OER in an electrolyte free of O_2, with the Pt ring settled at 0.4 V. At this potential the O_2 produced during the OER reaction will be reduced on the Pt ring and give a reducing current (see Figure S10).

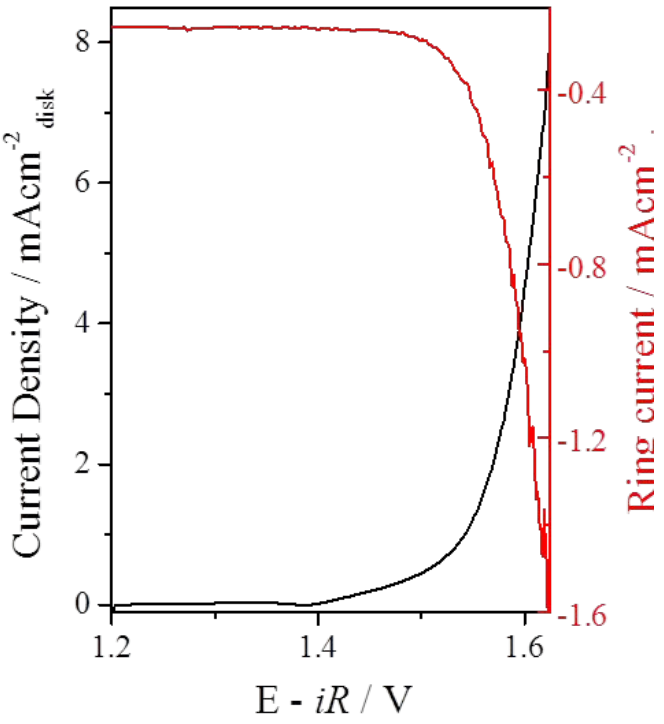

Figure S10. RRDE OER measurement with the Pt ring settled at 0.4 V to observe the reduction of the O_2 formed during the OER reaction.

S6. BET Surface Area

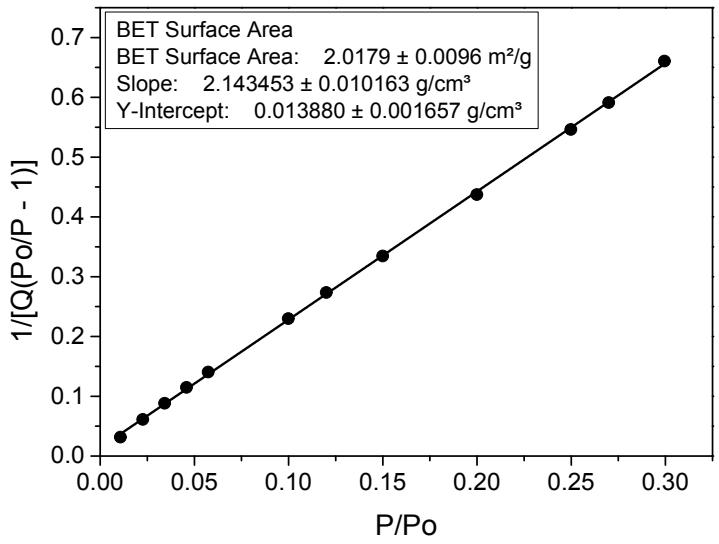

Figure S11: $La_{1.5}Sr_{0.5}NiMn_{0.5}Ru_{0.5}O_6$ BET surface area plot.

S7. Computational Details

We performed the DFT calculations with VASP,[8] with the projector augmented wave (PAW) approach,[9] the GGA-PBE exchange-correlation functional,[10] and Dudarev's DFT+U formalism[11] with U_{eff} values of 6.01 eV for Ni, 4.46 for Mn, and 6.70 for Ru ions. For Ni and Mn the values used are the average of those reported by Ceder and co-workers[12] for various Ni- and Mn-containing compounds. For Ru we used the value reported by Xu et al.[13]

We used 2×2 (001) perovskite slabs to simulate the surfaces (4 atomic layers thick: atoms in the topmost two layers and the adsorbates were fully relaxed, whereas the bottommost two were fixed at the equilibrium bulk distances, please refer to Figure S12), which contained four formula units in each case, with 4×4×1 k-point grids and a plane-wave cutoff of 450 eV. We added ~15 Å of vacuum in the z direction to avoid interactions between periodically repeated slabs. As shown in previous works, this setup suffices for the adsorption energies to be converged within 0.05 eV.[14-16]

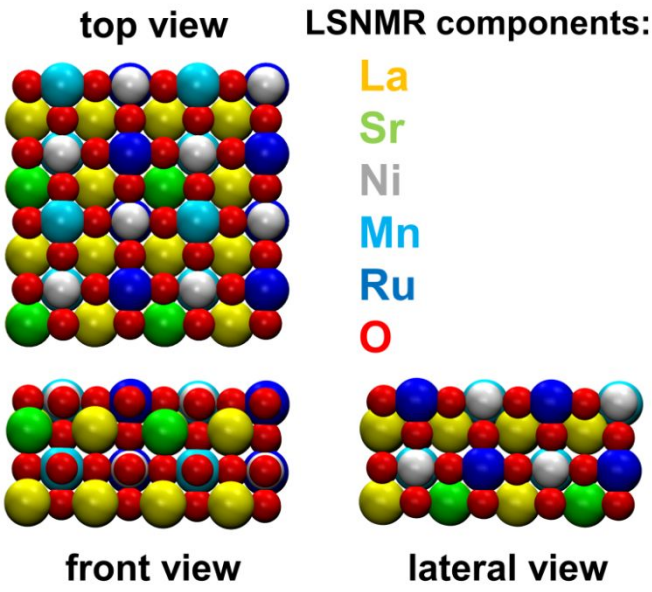

Figure S12. Top, front and side views of the LSNMR slabs under study. The colour code for each component is provided in the figure.

The calculations were made spin unrestricted in all cases. The relaxations were made with the conjugate-gradient scheme with k_BT = 0.01 eV and Gaussian smearing, taking the energies extrapolated to 0 K, until the maximal force on the relaxed atoms was 0.05 eV/Å. H_2O and H_2 were calculated in boxes of 15 Å × 15 Å × 15 Å and a 1×1×1 k-point grid with k_BT = 0.001 eV. The Gibbs energies were approximated as: $G \approx E_{DFT} + ZPE - TS$, where E_{DFT} and *ZPE* are the DFT-calculated total and zero-point energies respectively, while *TS* are entropic corrections for fluid-phase species. For H_2O(l) and H_2(g) the *TS* corrections are 0.67 and 0.40 at 298.15 K,[17] while the *ZPEs* for H_2O and H_2 are 0.58 and 0.28 eV.[17] The *ZPEs* for *O, *OH and *OOH are 0.07, 036 and 0.43 eV.

To describe the energetics of (H^++e^-) in terms of ½H_2(g) we used the computational hydrogen electrode.[18] Details on the construction of scaling-relation-based volcano plots appear elsewhere.[19] We assume that the OER mechanism is $OH^- \rightarrow *OH \rightarrow *O \rightarrow *OOH \rightarrow O_2$. The OER overpotential is calculated as:

$$\eta_{OER} = \max\left(\Delta G_1, \Delta G_2, \Delta G_3, \Delta G_4\right)/e - E^0 \qquad \text{(S6)}$$

where $\Delta G_1 = \Delta G_{OH}$, $\Delta G_2 = \Delta G_O - \Delta G_{OH}$, $\Delta G_3 = \Delta G_{OOH} - \Delta G_O$, $\Delta G_4 = 4E^0 - \Delta G_{OOH}$, and $E^0 = 1.23$ V is the equilibrium potential of the reaction. Note that ΔG_O is the reaction energy of $* + H_2O \rightarrow *O + 2H^+ + 2e^-$, ΔG_{OH} is the reaction energy of $* + H_2O \rightarrow *OH + H^+ + e^-$, and ΔG_{OOH} is in turn the reaction energy of

$* + 2H_2O \rightarrow *OOH + 3H^+ + 3e^-$. From the acid-based reference of the adsorption energies to the alkaline one is based on the reaction $H_2O \rightarrow H^+ + OH^-$, which has a free energy of 0.83 eV. Note that the use of either scale has no influence on the predicted overpotentials. The electrochemical-step symmetry index (ESSI) is defined as follows for the OER:[20]

$$ESSI = \left(\frac{1}{n} \sum_i^n \Delta G_i^* \right) - E^0 \quad \text{(S7)}$$

where ΔG_i^* are the adsorption energies in ΔG_1 to ΔG_4 larger than $E^0 = 1.23$ V. For instance, the adsorption energies of *O, *OH, and *OOH for Ru sites at LSNMR (Ru @ LSNMR) are 2.27, 0.54, and 3.89 eV, according to Table S3. 0.54, 1.73, 1.62 and 1.03 eV, so that the overpotential is $\eta_{OER}^{LSNMR} = 1.73 - 1.23 = 0.50$ V and $ESSI_{OER}^{LSNMR} = (1.73 + 1.62)/2 - 1.23 = 0.44$ V.

If the ORR is assumed to proceed as: $O_2 \rightarrow *OOH \rightarrow *O \rightarrow *OH \rightarrow OH^-$, one can make an analogous analysis so as to be able to calculate η_{ORR}, $ESSI_{ORR}$[20] and the bifunctional index as:

$$BI = \eta_{OER} + \eta_{ORR} \quad \text{(S8)}$$

Table S3 contains ΔG_O, ΔG_{OH}, ΔG_{OOH}, $ESSI_{OER}$, $ESSI_{ORR}$, η_{OER} and η_{ORR} for the different sites on LSNMR.

Table S3. Adsorption energies (eV) of *O, *OH and *OOH on the different sites of LSNMR, ESSI values (V) and calculated overpotentials (V) for the OER and the ORR. The values in bold are used to determine the BI of LSNMR.

description	ΔG_O	ΔG_{OH}	ΔG_{OOH}	$ESSI_{OER}$	η_{OER}	$ESSI_{ORR}$	η_{ORR}
Ni@LSNMR	3.71	1.47	4.41	0.62	1.01	-0.62	0.72
Mn@LSNMR	3.12	0.96	4.08	0.93	0.93	**-0.31**	**0.39**
Ru@LSNMR	2.27	0.54	3.89	**0.44**	**0.50**	-0.44	0.69

In Figure S13 we provide the correlation between $\Delta ESSI = ESSI_{OER} - ESSI_{ORR}$ and BI for Ru, Ni and Mn sites at LSNMR, the best combination of those made from Mn sites for the ORR and Ru sites for the OER, and additional data from the literature for other oxides: RuO_2,[16] IrO_2,[16] MnO_x,[16] Co_xO_y,[16, 21] and Pt(111)/PtO_2.[16, 22] For Pt(111) we extrapolated the data in ref.[22] from the fully solvated environment to the onset potential conditions where high adsorbate coverages are expected to weaken the adsorption energies of *O, *OH and *OOH at least by ~0.4, 0.19 and 0.17 eV. Following the surface Pourbaix

diagrams, for Co_xO_y we used the OER data for CoOOH and the ORR data for Co_3O_4. Likewise, for MnO_x we used the OER data for MnO_2 and the ORR data for Mn_2O_3. The mean absolute error (MAE) between the linear fit and the data is only 0.10 V. The experimental data in the inset of Figure 4 in the main text was taken from this study for LSNMR and from various references for the other materials (RuO_2,[23-24] MnO_x,[24] Pt/C,[25] IrO_2,[25] Co_yO_x[23]).

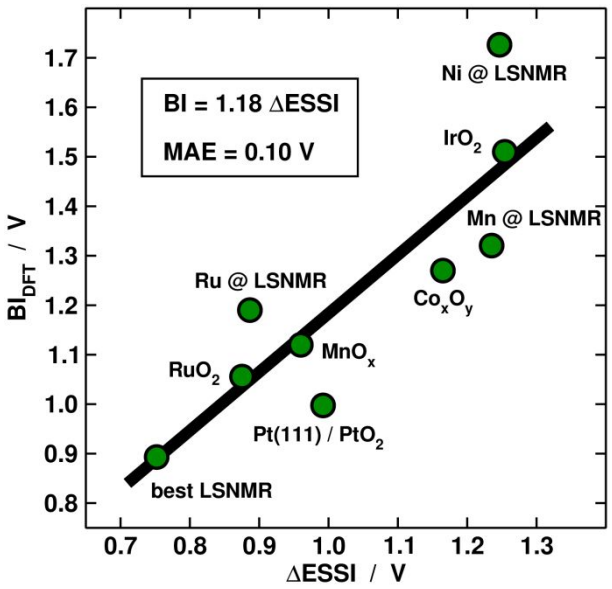

Figure S13. Correlation between ΔESSI and the DFT-calculated BI for several electrocatalysts in this study and the literature (see this SI for the data sources).

S8. Post Mortem TEM Study

S8.1. Postmortem ORR study

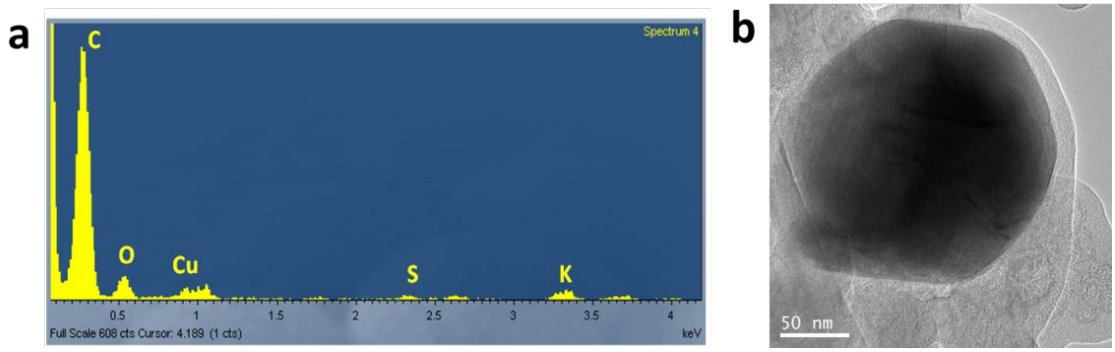

Figure S14. a) EDX of the amorphous regions around the perovskite particles. b) TEM of a particle covered by carbon.

S8.2. Postmortem OER study

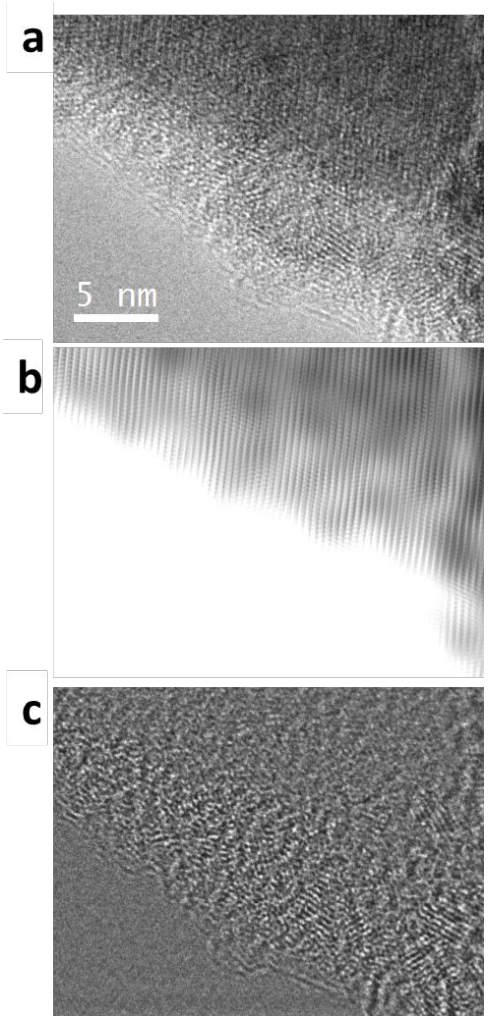

Figure S15. a) HR-TEM image of an isolated degraded particle after 500 OER cycles. b) FFT filtered image of the HR-TEM using only the reflections corresponding to the perovskite, showing that the periodicity of the structure is maintained in the bulk, and c) filtered image of the HR-TEM with the rest of reflections, indicating the presences of nanoparticles and high disorder mainly at 5-10 nm in the surface.

References

1. Sahiner, A.; Croft, M.; Guha, S.; Perez, I. I.; Zhang, Z.; Greenblatt, M.; Metcalf, P. A.; Jahns, H.; Liang, G., Polarized Xas Studies of Ternary Nickel Oxides. *Phys Rev B Condens Matter.* **1995,** *51* (9), 5879-5886.
2. Mandal, T. K.; Croft, M.; Hadermann, J.; Van Tendeloo, G.; Stephens, P. W.; Greenblatt, M., La_2MnVO_6 Double Perovskite: a Structural, Magnetic and X-ray Absorption Investigation. *Journal of Materials Chemistry* **2009,** *19* (25), 4382.
3. Bune, R. O.; Lobanov, M. V.; Popov, G.; Greenblatt, M.; Botez, C. E.; Stephens, P. W.; Croft, M.; Hadermann, J.; Tendeloo, G. V., Crystal Structure and Properties of Ru-Stoichiometric $LaSrMnRuO_6$. *Chem. Mater.* **2006,** *18*, 2611-2617.
4. Retuerto, M.; Li, M.-R.; Go, Y.; Ignatov, A.; Croft, M.; Ramanujachary, K.; Hadermann, J.; Hodges, J.; Herber, R.; Nowik, I., Magnetic and Structural Studies of the Multifunctional Material $SrFe_{0.75}Mo_{0.25}O_{3-\delta}$. *Inorganic chemistry* **2012,** *51* (22), 12273-12280.
5. Groot, F. M. F. d.; Z. W. Hu; Lopez, M. F.; Kaindl, G.; Guillot, F.; Tronc, M., Differences Between L_3 and L_2 X-Ray Absorption Spectra of Transition Metal Compounds. *J. Chem. Phys.* **1994,** *101* (8), 6570-6576.
6. Hu, Z.; Lips, H. v.; Golden, M. S.; Fink, J.; Kaindl, G.; Groot, F. M. F. d.; Ebbinghaus, S.; Reller, A., Multiplet Effects in the Ru-$L_{2,3}$ X-Ray Absorption Spectra of Ru(IV) and Ru(V) Compounds. *Physical Review B* **2000,** *61* (8), 5262.
7. McCrory, C. C.; Jung, S.; Peters, J. C.; Jaramillo, T. F., Benchmarking Heterogeneous Electrocatalysts for the Oxygen Evolution Reaction. *J Am Chem Soc* **2013,** *135* (45), 16977-87.
8. Kresse, G.; Furthmüller, J., Efficient Iterative Schemes for Ab Initio Total-Energy Calculations Using a Plane-Wave Basis Set. *Physical Review B* **1996,** *54* (16), 11169-11186.
9. Kresse, G.; Joubert, D., From Ultrasoft Pseudopotentials to the Projector Augmented-Wave Method. *Physical Review B* **1999,** *59* (3), 1758-1775.
10. Perdew, J. P.; Burke, K.; Ernzerhof, M., Generalized Gradient Approximation Made Simple. *Physical Review Letters* **1996,** *77* (18), 3865-3868.
11. Dudarev, S. L.; Botton, G. A.; Savrasov, S. Y.; Humphreys, C. J.; Sutton, A. P., Electron-Energy-Loss Spectra and the Structural Stability of Nickel Oxide: An LSDA+U study. *Physical Review B* **1998,** *57* (3), 1505-1509.
12. Zhou, F.; Cococcioni, M.; Marianetti, C. A.; Morgan, D.; Ceder, G., First-Principles Prediction of Redox Potentials in Transition-Metal Compounds With LDA+U. *Physical Review B* **2004,** *70* (23), 235121.
13. Xu, Z.; Rossmeisl, J.; Kitchin, J. R., A Linear Response DFT+U Study of Trends in the Oxygen Evolution Activity of Transition Metal Rutile Dioxides. *J. Phys. Chem. C* **2015,** *119* (9), 4827-4833.
14. Calle-Vallejo, F.; Inoglu, N. G.; Su, H.-Y.; Martínez, J. I.; Man, I. C.; Koper, M. T. M.; Kitchin, J. R.; Rossmeisl, J., Number of Outer Electrons as Descriptor for Adsorption Processes on Transition Metals and Their Oxides. *Chemical Science* **2013,** *4* (3), 1245.
15. Calle-Vallejo, F.; Díaz-Morales, O. A.; Kolb, M. J.; Koper, M. T. M., Why Is Bulk Thermochemistry a Good Descriptor for the Electrocatalytic Activity of Transition Metal Oxides? *ACS Catal.* **2015,** *5* (2), 869-873.
16. Man, I. C.; Su, H.-Y.; Calle-Vallejo, F.; Hansen, H. A.; Martinez, J. I.; Inoglu, N. G.; Kitchin, J.; Jaramillo, T. F.; Norskov, J. K.; Rossmeisl, J., Universality in Oxygen Evolution Electrocatalysis on Oxide Surfaces. *ChemCatChem* **2011,** *3* (7), 1159-1165.
17. Briquet, L. G. V.; Sarwar, M.; Mugo, J.; Jones, G.; Calle-Vallejo, F., A New Type of Scaling Relations to Assess the Accuracy of Computational Predictions of Catalytic Activities Applied to the Oxygen Evolution Reaction. *ChemCatChem* **2017,** *9* (7), 1261-1268.
18. Nørskov, J. K.; Rossmeisl, J.; Logadottir, A.; Lindqvist, L.; Kitchin, J. R.; Bligaard, T.; Jónsson, H., Origin of the Overpotential for Oxygen Reduction at a Fuel-Cell Cathode. *J. Phys. Chem. B* **2004,** *108* (46), 17886-17892.
19. Calle-Vallejo, F.; Koper, M. T. M., First-Principles Computational Electrochemistry: Achievements and Challenges. *Electrochimica Acta* **2012,** *84*, 3-11.

20. Govindarajan, N.; García-Lastra, J. M.; Meijer, E. J.; Calle-Vallejo, F., Does the Breaking of Adsorption-Energy Scaling Relations Guarantee Enhanced Electrocatalysis? *Current Opinion in Electrochemistry* **2018,** *8*, 110-117.
21. Bajdich, M.; García-Mota, M.; Vojvodic, A.; Nørskov, J. K.; Bell, A. T., Theoretical Investigation of the Activity of Cobalt Oxides for the Electrochemical Oxidation of Water. *J. Am. Chem. Soc.* **2013,** *135* (36), 13521-13530.
22. Calle-Vallejo, F.; Tymoczko, J.; Colic, V.; Vu, Q. H.; Pohl, M. D.; Morgenstern, K.; Loffreda, D.; Sautet, P.; Schuhmann, W.; Bandarenka, A. S., Finding Optimal Surface Sites on Heterogeneous Catalysts by Counting Nearest Neighbors. *Science* **2015,** *350* (6257), 185.
23. Masa, J.; Xia, W.; Sinev, I.; Zhao, A.; Sun, Z.; Grützke, S.; Weide, P.; Muhler, M.; Schuhmann, W., Mn_xO_y/NC and Co_xO_y/NC Nanoparticles Embedded in a Nitrogen-Doped Carbon Matrix for High-Performance Bifunctional Oxygen Electrodes. *Angewandte Chemie International Edition* **2014,** *53* (32), 8508-8512.
24. Su, H.-Y.; Gorlin, Y.; Man, I. C.; Calle-Vallejo, F.; Nørskov, J. K.; Jaramillo, T. F.; Rossmeisl, J., Identifying Active Surface Phases for Metal Oxide Electrocatalysts: a Study of Manganese Oxide Bi-Functional Catalysts for Oxygen Reduction and Water Oxidation Catalysis. *Phys. Chem. Chem. Phys.* **2012,** *14* (40), 14010-14022.
25. Aijaz, A.; Masa, J.; Rösler, C.; Xia, W.; Weide, P.; Botz, A. J. R.; Fischer, R. A.; Schuhmann, W.; Muhler, M., $Co@Co_3O_4$ Encapsulated in Carbon Nanotube-Grafted Nitrogen-Doped Carbon Polyhedra as an Advanced Bifunctional Oxygen Electrode. *Angewandte Chemie International Edition* **2016,** *55* (12), 4087-4091.